

A Review of Artificial Intelligence in Brachytherapy

Jingchu Chen^{1,2}, Richard L.J. Qiu¹, Tonghe Wang³, Shadab Momin¹ and Xiaofeng Yang^{1*}

¹Department of Radiation Oncology and Winship Cancer Institute, Emory University, Atlanta, GA 30308

²School of Mechanical Engineering, Georgia Institute of Technology, GA, Atlanta, USA

³Department of Medical Physics, Memorial Sloan Kettering Cancer Center, New York, NY 10065

*Corresponding author:

Xiaofeng Yang, PhD

Department of Radiation Oncology

Emory University School of Medicine

1365 Clifton Road NE

Atlanta, GA 30322

E-mail: xiaofeng.yang@emory.edu

Abstract

Artificial intelligence (AI) has the potential to revolutionize brachytherapy's clinical workflow. This review comprehensively examines the application of AI, focusing on machine learning and deep learning, in facilitating various aspects of brachytherapy. We analyze AI's role in making brachytherapy treatments more personalized, efficient, and effective. The applications are systematically categorized into seven categories: imaging, preplanning, treatment planning, applicator reconstruction, quality assurance, outcome prediction, and real-time monitoring. Each major category is further subdivided based on cancer type or specific tasks, with detailed summaries of models, data sizes, and results presented in corresponding tables. This review offers insights into the current advancements, challenges, and the impact of AI on treatment paradigms, encouraging further research to expand its clinical utility.

Keywords: AI, machine learning, brachytherapy, HDR, LDR

1 INTRODUCTION

Brachytherapy is a form of internal radiation therapy that is delivered with either low dose rate (LDR) or high dose rate (HDR). It involves the direct placement of radioactive sources within or near the tumor via applicators. Brachytherapy plays a crucial role in radiation therapy due to its ability to deliver high and conformal radiation doses to the tumor with reduced dose to adjacent organ-at-risk (OARs), thereby offering an advantageous therapeutic ratio. [13, 20, 75, 111, 117]

After patient consultation and consent for treatment, both LDR and HDR, forms of brachytherapy procedures, may contain several key steps: (a) Preplanning diagnostic imaging; (b) Surgical insertion of needles, applicators, or catheters; (c) Treatment planning imaging and verification; (d) Image registration and segmentation; (e) Applicators/catheters reconstruction; (d) Treatment planning; (f) Quality assurance (QA); (g) Treatment delivery; (h) Patient follow up.

Overall workflow for brachytherapy procedures can be labor and resource intensive for personnel involved from different disciplines. However, efficiency and efficacy of brachytherapy procedures is

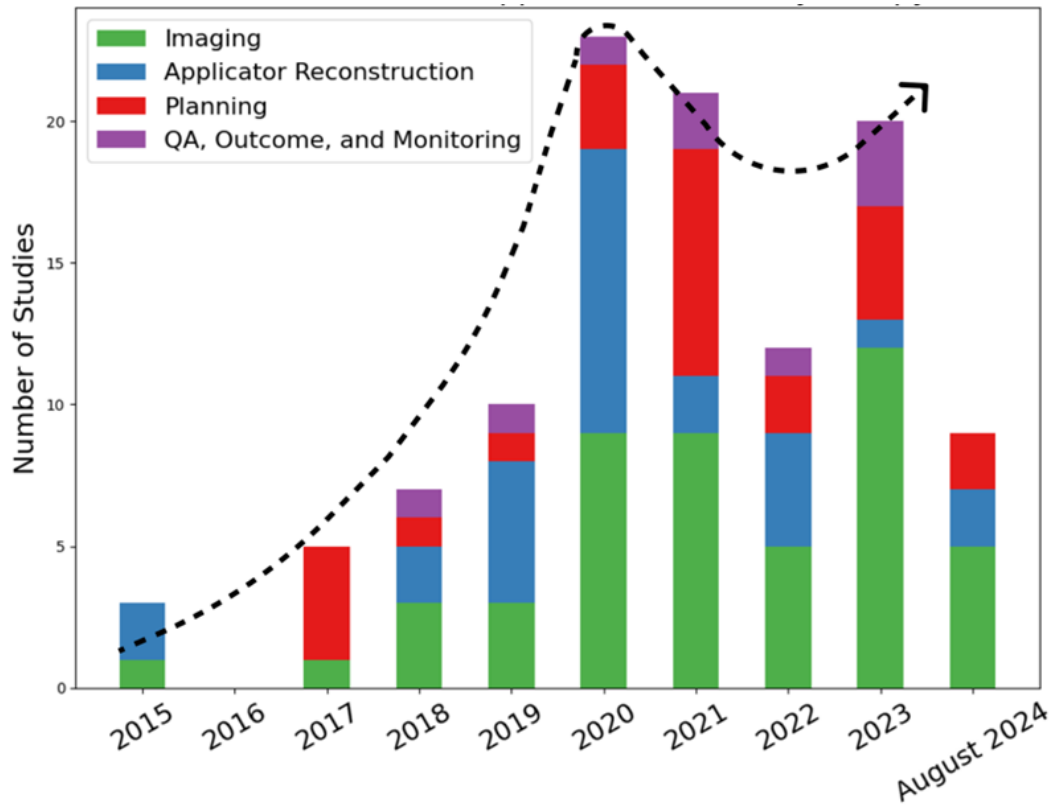


Figure 1. Overview of the number of studies in applications of AI in brachytherapy from 2015 to August 2024 with an approximate dotted trendline. 'Imaging' combines the image registration, image segmentation, and other imaging-related tasks. 'Planning' includes both preplanning and treatment planning. 'Applicator reconstruction' includes both prostate and gynecologic cancer-related applicator reconstructions including needles, catheters, and seeds. 'QA, Outcome, and Monitoring' combined the remaining three categories because of their relatively small number of studies.

highly dependent on the clinician's skills and level of experience owing to their involvement at various points in the workflow including diagnostics, implantation, and treatment planning. With the goal of further improving the efficiency and addressing the challenges present in brachytherapy procedures, studies have integrated artificial intelligence (AI) to facilitate these procedures. In recent years, it has become clear that AI, which could be considered the fourth industrial revolution, is emerging as a transformative force across various sectors, including healthcare. [98, 109] Radiation oncology and medical physics, disciplines at the forefront of integrating cutting-edge scientific and technological innovations, are increasingly exploring the potential of AI to revolutionize treatment paradigms. [29, 52, 94] Within the realm of AI, Machine learning (ML) relies on statistical models to learn from previous data and make predictive decisions, which can be useful in selecting brachytherapy applicators and predicting outcomes. [1, 27, 113, 118, 125] Deep learning (DL), a subset of ML, uses neural networks such as Convolutional Neural Network (CNN) [89] and Generative Adversarial Network (GAN) [36] to execute complex image analysis tasks [134], which are fundamentally involved in most of the brachytherapy workflow. [44]

Figure 1 shows the number of studies that utilized AI for different brachytherapy purposes from 2015 up to August 2024. After a significant increase in the number of studies on AI applications in brachytherapy up to 2020, there is a stagnation in the growth of these studies in the subsequent years (Figure 1). Given the rapid advancements and the potentials of AI to refine and redefine brachytherapy treatment workflow, a comprehensive review of the current and emerging applications of AI in the context of brachytherapy is both timely and pivotal to encourage more researchers to study brachytherapy and to provide physicians with an overview of the current state of AI in brachytherapy. Therefore, we collected recent developments in the applications of AI in different brachytherapy procedures to provide a detailed analysis of the potentials of AI in leading to more personalized, efficient, and effective brachytherapy treatments.

■ Imaging ■ Planning ■ QA, Outcome, Monitoring ■ Applicator Reconstruction

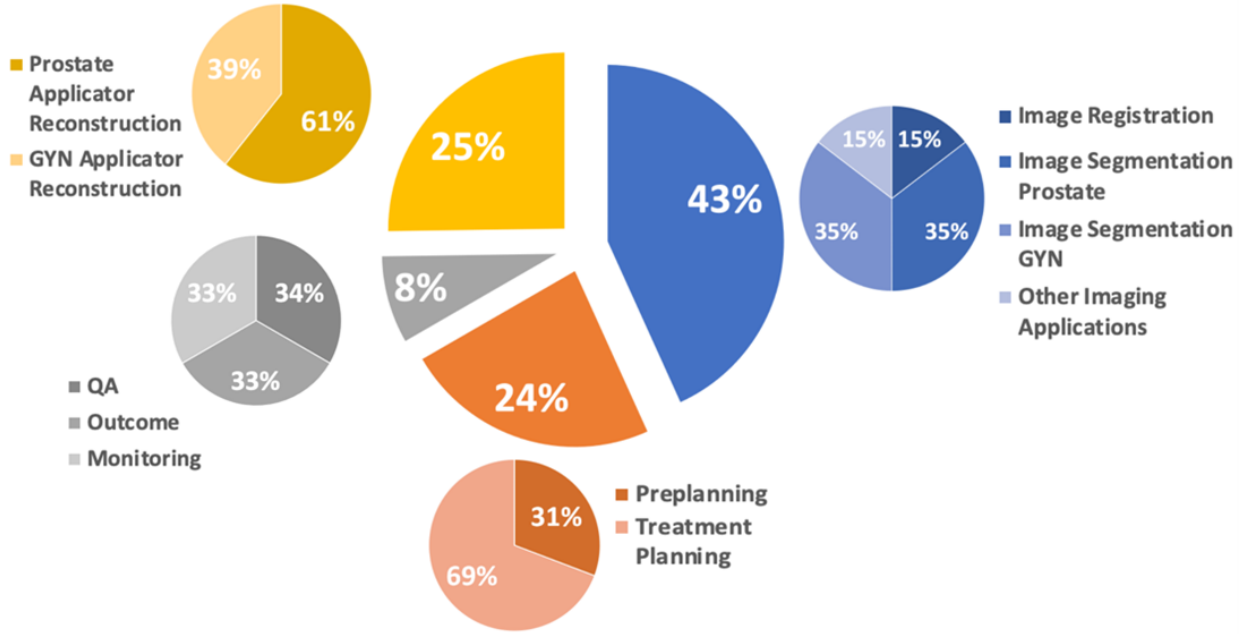


Figure 2. Percentage pie chart of applications of AI in different procedures in brachytherapy.

The literature search was conducted in August 2024, initially retrieving 205 papers from PubMed using the keywords "brachytherapy", combined with "artificial intelligence", "deep learning", or "machine learning". Additional papers were supplemented from The American Association of Physicists in Medicine (AAPM) and Google Scholar by searching the same keywords. A total of 111 studies were selected and thoroughly reviewed. The innovative approaches used to develop each unique AI model, along with their corresponding performances, are presented and categorized by different clinical procedures in brachytherapy workflow, with further sub-categorization based on specific organs or detailed applications.

The studies are categorized into 7 sections: imaging (section 2), preplanning (section 3), treatment planning (section 4), applicator reconstruction (section 5), QA (section 6), outcome prediction (section 7), and real-time monitoring (section 8). The detailed percentage distribution of these studies is illustrated in Figure 2.

Below is a summary of several common evaluation methods used in the literature for evaluating the performance of the AI models.

1. The Dice Similarity Coefficient (DSC) is the most used metric for measuring the overlap ratio of between the automatic (A) and ground truth (B) contours.

$$DSC = \frac{2 \times (A \cap B)}{|A| + |B|}, \quad (1)$$

2. Hausdorff Distance (HD) measures the maximum distance between points in the predicted segmentation and points in the ground truth images, serving as a measure of dissimilarity. HD95, commonly used in many studies, disregards outliers by considering only the 95th percentile of HD.

$$HD_{95} = \max\{\sup_{k^{95\%}} \inf_{a \in A} \inf_{b \in B} d(a, b), \sup_{b \in B} \inf_{a \in A} d(a, b)\}, \quad (2)$$

where: a are the points belong to image set A, and b are the points belong to image set B.

3. Mean Surface Distance (MSD) compares the average difference between the surface of automatic segmentation (A) and ground truth contours (B).

$$MSD = \frac{1}{A} \sum_{a \in A} \min_{b \in B} |a - b| + \frac{1}{B} \sum_{b \in B} \min_{a \in A} |b - a|, \quad (3)$$

where: a are the points belong to image set A, and b are the points belong to image set B.

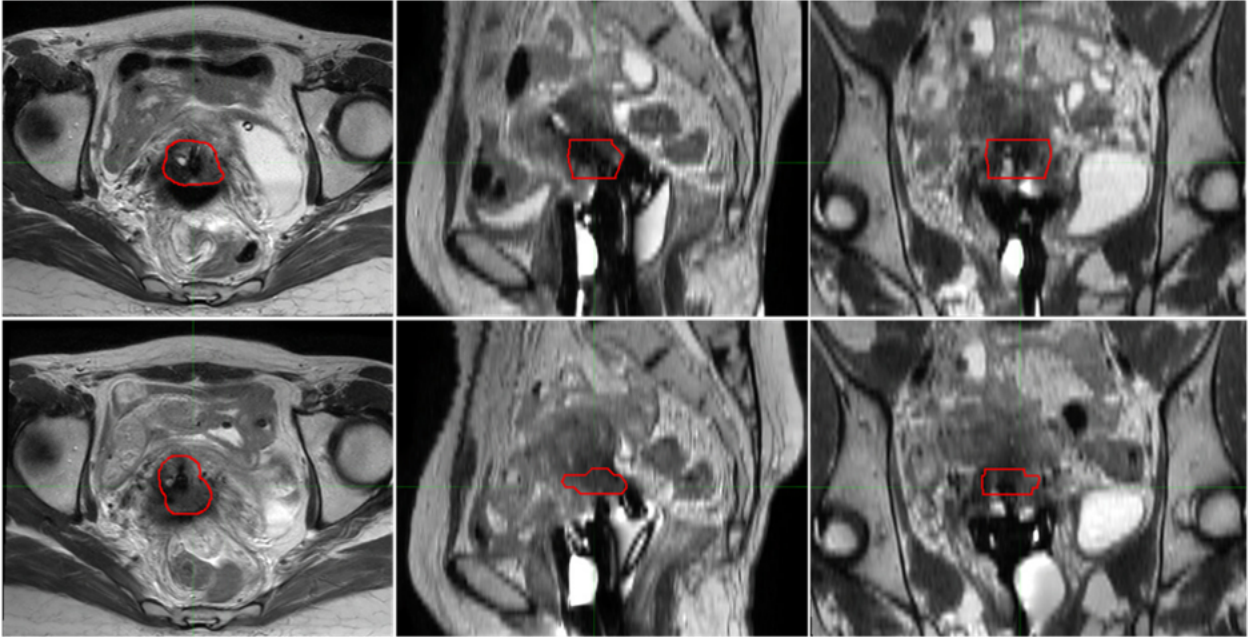


Figure 3: Inter-fractional changes in gynecologic brachytherapy. The red circle indicates the GTV. The images display axial (left column), sagittal (middle column), and coronal (right column) views, demonstrating the variations observed across two treatment fractions with one week interval (upper and lower rows).

2 Imaging

Many modern imaging models use CNN [89] or fully convolutional networks (FCN) [74], which incorporate spatial information to perform pixel-wise classification for computer vision tasks. Ronneberger et al. [102] built the first U-Net structure based on FCN specifically for biomedical image segmentation. The U-Net model specializes in biomedical image segmentation because of its incorporation of data augmentation with elastic deformation, which reduces the need for large training dataset. This model also addresses tissue deformation variability through elastic deformation data augmentation. Several models use U-Net as a backbone, enhancing segmentation results with additional multiple skip connections between encoder levels and self-adapting frameworks, such as Unet++ [152] and nnU-Net (no-new-net) [53]. Additionally, U-Net can be combined with Transformers, such as the TransUNet [15] and UNETR (UNET Transformers) [41], which use local semantic and texture information while incorporating long-range dependencies among pixels [42]. Since imaging is a crucial element in brachytherapy, the neural network-based models and their variations are extensively employed to perform image registration, image segmentation, and other applications.

2.1 Image Registration

Image registration is the process of aligning multimodality medical images or the single modality medical images between different treatment fractions in brachytherapy. Table 1 provides an overview of the methods and results from current AI-based image registration implementations.

Gynecologic (GYN) brachytherapy typically involves multiple treatment fractions, during which organ deformation occurs due to varying bladder and rectum filling, applicator insertion, and inter-fractional tumor changes [115]. Figure 3 illustrates the inter-fractional changes of the gross tumor volume (GTV), which is labeled in red, in GYN brachytherapy. Organ deformations cause dosimetric uncertainty for the target and OARs, making image registration necessary. The transformation in image registration can be subdivided into rigid, affine, and deformable, while the registration method can be either intensity-based or geometric-based.

To address inter-fractional changes of organs involved in GYN brachytherapy, Salehi et al. [103] developed a deep learning-based non-rigid deformable image registration algorithm (DIRNet) for aligning

CT images of the cervix and OARs. By fixing the bony structures and applying deformed binary masks for the organs, the study showed that DIRNet achieved comparable results in the DSC and significantly better Jaccard distance (JI) – the ratio of the intersected region relative to the union of the automatic and ground truth contours - and MSD than the conventional intensity-based image registration (SimpleElastix), as detailed in Table 1. Besides deformable image registration, rigid registration can be performed based on applicator geometries. Ecker et al. [26] combined deep learning-based applicator segmentation with existing rigid registration methods to automate the registration between MR-guided GYN brachytherapy fractions. A 3D UNETR model was used to segment applicators with a DSC of 0.70 ± 0.07 and served as the reference for rigid registration. The mean distance error (MDE) of registration using the predicted segmentation was 2.7 ± 1.4 mm, which is relatively high compared to the error using ground truth segmentation, which was only 0.7 ± 0.5 mm. Although the current registration error remains above the desired registration error of 2 mm, this discrepancy is likely due to the limited segmentation accuracy of applicators. The study demonstrated that if a segmentation method that produces similar results as the ground truth is used, the registration error can be reduced, achieving an automated registration process significantly faster than manual methods.

In prostate brachytherapy, image registration is crucial for fusing organ information between multiple image modalities. Transrectal ultrasound (TRUS) is often used for guiding the insertion of needles or catheters in prostate brachytherapy, while MRI offers greater soft tissue contrasts compared to TRUS. The incorporation of knowledge from MRI into TRUS images can thus provide additional soft tissue guidance. However, registering MRI to TRUS images remains challenging due to the limited availability of ground truth deformation of the prostate.

To address this challenge, several different AI-based methods are provided. Zeng et al. [145] developed a fully automated deep learning system based on a weakly supervised method, which trains models using only partially labeled data. The entire workflow could be summarized into three steps: initial segmentation on TRUS and MRI using two FCNs, affine registration using a 2D CNN, and non-rigid registration using 3D U-Net based network. The initial segmentation results produced reliable results for the registration, where the DSC = 0.88 ± 0.05 and 0.92 ± 0.03 for the MRI and for TRUS. The affine and non-rigid registration methods were followed using MRI-TRUS labels (SR-L) and MRI-TRUS images (SR-I) as inputs. Overall, the model produced the best DSC, mean target registration error, mean MSD, and HD using the SR-L input method, with DSC = 0.91 ± 0.02 , target registration error = 2.53 ± 1.39 mm, MSD = 0.88 mm, and HD = 4.41 mm. Using the labels as input and deep-learning methods for initialization, Zeng’s approach showed high accuracy in automatic registration of MRI-TRUS images of prostate.

Besides the label-based method, Chen et al. [17] provided a segmentation-based method, which used 3D V-Net models to segment the prostate after catheter insertion on MR and US images, align the centroids, and probability maps to predict deformable displacement fields. Despite the presence of catheter artifacts in the images, the model achieved a DSC of 0.87 ± 0.05 , a Center of Mass distance error of 1.7 ± 0.89 mm, an HD of 7.21 ± 2.07 mm, and an MSD of 1.61 ± 0.64 mm. The segmentation-based method provided slightly inferior results than the label-based method, likely due to the results of initial segmentation (DSC values of 0.86 ± 0.05 and 0.90 ± 0.03 on MR and US) and utilization of hierarchical information of anatomy rather than image intensities. While current studies have shown positive outcomes when integrating MRI into TRUS-based workflows, using MRI-registered contours, whether rigid, semi-rigid, or deformable, may still lead to significant dose under-coverage. [107]

2.2 Image Segmentation

Image segmentation involves defining various target volumes that require treatment and OARs that require sparing during brachytherapy. It serves as the foundation for various tasks in the brachytherapy workflow including treatment planning. We summarized the AI segmentation methods and results for GYN-related tasks in Table 2 and for prostate-related tasks in Table 3.

2.2.1 GYN

The GYN-related segmentation studies focused on segmenting the GTV, the high-risk clinical target volume (HR-CTV) which extends from the GTV to account for possible microscopic spread of cancer,

TABLE I. AI applications in image registration

Cancer Site	Image Modality	Registration Method	Number of Patients	Model	Result Summary	Citation
GYN	CT	Non-rigid	57	DIRNet	Mean MSD (mm): Model = 1.61 ± 0.46 , 1.17 ± 0.15 , 1.06 ± 0.42 ; SimpleElastix = 2.94 ± 0.78 , 3.26 ± 0.74 , 3.04 ± 1.50 (cervix, bladder, rectum). Mean MSD (mm): Model = 1.61 ± 0.46 , 1.17 ± 0.15 , 1.06 ± 0.42 ; SimpleElastix = 2.94 ± 0.78 , 3.26 ± 0.74 , 3.04 ± 1.50 (cervix, bladder, rectum). Mean JI: Model = $86 \pm 4\%$, $93 \pm 1\%$, $88 \pm 4\%$; SimpleElastix = $71 \pm 8\%$, $83 \pm 4\%$, $67 \pm 11\%$ (cervix, bladder, rectum).	[103]
GYN	MRI	Rigid	56	2D U-Net and 3D UNETR	MDE between dwell positions = 2.7 ± 1.4 mm.	[26]
Prostate	MRI-TRUS	Affine and non-rigid	36	FCN, 2D CNN, and 3D U-Net	DSC = 0.91 ± 0.02 , target registration error = 2.53 ± 1.39 mm, MSD = 0.88 mm, and HD = 4.41 mm.	[145]
Prostate	MRI-TRUS	Affine and non-rigid	32	FCN and RNN	DSC = 0.90 ± 0.04 , target registration error = 2.77 ± 1.40 mm.	[141]
Prostate	MRI-TRUS	Rigid	121	3D V-Net and Probability Maps	DSC = 0.87 ± 0.05 , Center of Mass distance error = 1.7 ± 0.89 mm, HD = 7.21 ± 2.07 mm, and MSD = 1.61 ± 0.64 mm.	[17]
Prostate	MRI-TRUS	Deformable	642	Weakly-supervised Volumetric Registration	DSC = 0.873 ± 0.113 , HD = 4.56 ± 1.95 mm, and MSD = 0.053 ± 0.026 mm.	[131]
Prostate	MRI-TRUS	Rigid	662	Attention-Reg	DSC = 0.82 ± 0.06 and Surface Registration Error = 5.99 ± 3.52 mm.	[112]

Note: Abbreviations: RNN (recurrent neural network).

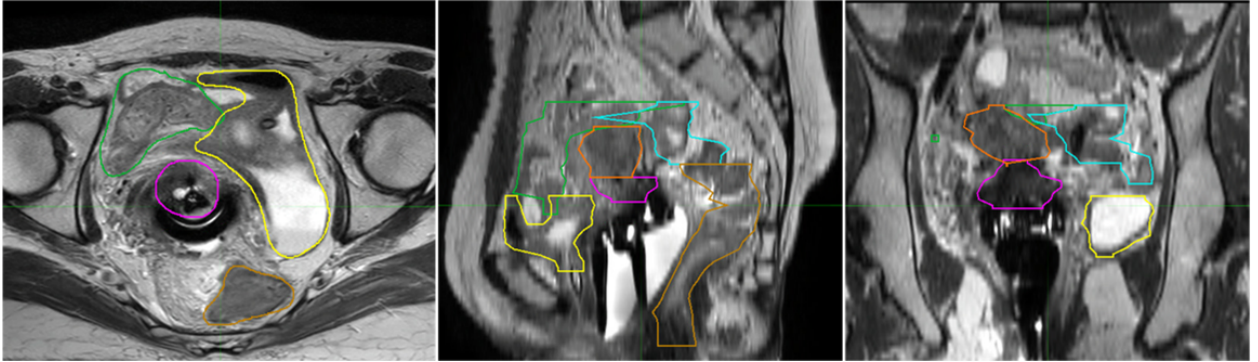


Figure 4: Image segmentation on MRI for a GYN brachytherapy patient, showing axial, sagittal, and coronal views. The segmented structures are indicated by different colors: magenta for the cervix, yellow for the bladder, green for the bowel, orange for the uterus, gold for the rectum, and blue for the recto sigmoid.

and the OARs including bladder, rectum, sigmoid, and small intestine. As shown in Figure 4, various structures need to be considered for GYN brachytherapy patients.

Incorporating MRI into image-guided brachytherapy treatment planning enhances the clarity of targets and OARs. However, contouring organs on MRI is a labor-intensive process, especially problematic when performed while the patient is immobilized with the applicator inserted during brachytherapy. For this reason, several studies aim at developing an automated method for GYN organ segmentation on MRI post applicator insertion. Yoganathan et al. [135] trained two deep CNN architectures, a residual neural network (ResNet50) and an inception residual network (InRN) to automatically segment the GTV, HR-CTV, and the OARs on MRI scans for patients with Foleys catheter inserted. The GTV often appears in non-uniform shapes and variable sizes, which makes it challenging to identify. The study implemented a 2.5D method that utilizes axial, sagittal, and coronal views to include additional contextual spatial information. Combining 2.5D model with InRN network architecture yielded optimal segmentation results as detailed in Table 2. However, MRI scans exhibit variations due to different clinical setting, such as different scanners vendors, scanning parameters, and applicator types. To enhance model robustness and adaptability to various applicators and MRI scanners, two studies incorporated diverse settings in their training data, aiming to develop a more generalized model. Zabihollahy et al.

[140] trained a 2-step CNN (3D Dense U-Net) with different MRI setups: MR1 with a repetition time (TR) of 2600 ms and time to echo (TE) of 95 ms, and MR2 with a TR of 3500 ms and TE of 97 ms. Ni et al. [82] fine-tuned a pre-trained model with diverse training groups mixing different MRI scanners (1.5T Siemens Espree and 3T Siemens Verio) and brachytherapy applicators (tandem and ring, Syed-Neblett template, Venezia applicator). The optimal segmentation results of OARs from both studies suggest that training with mixed data improves generalizability, making the models more viable for future clinical implementation. The rapid segmentation of AI models can also facilitate MRI-guided brachytherapy planning. Kim et al. [61] developed a dual convolution-transformer U-Net (DCT-UNet) that provided HR-CTV and OAR segmentation along with a real-time active needle tracking function to enhance the efficiency of MRI-guided brachytherapy procedures. The model is also incorporated into the treatment planning system (TPS), to assist radiation oncologists in precisely placing catheters under MRI guidance. The approach involved deformably registering the MRI from the primary treatment planning image with contours (T2SPACE) to the MRI acquired during the procedure (T2QM), enabling accurate and real-time tracking for improved guidance. The model achieved high DSC scores for OAR segmentations, despite having less optimal results for the HR-CTV on T2QM. This demonstrates its potential for improving catheter placement in MRI-guided brachytherapy.

CT has been extensively used in image-guided adaptive brachytherapy, facing similar time-constraint challenges as MRI. Several studies have employed neural network-based models to simultaneously segment HR-CTV and OARs on CT images [25, 56, 70, 124, 133, 146, 153]. Li et al. [70], Duprez et al. [25], and Xue et al. [133] employed nnU-Net-based models to segment HR-CTV and OARs across various configurations, including 2D U-Net, 3D U-Net, and 3D Cascade U-Net. Unlike regular U-Net, the nnU-Net handles training parameters autonomously for new tasks and each segmentation task uses the best corresponding architecture. Li and Duprez's studies produced similar results in terms of DSC, HD95, and MSD with the 3D Cascade U-Net configuration in nnU-Net. However, Xue's study incorporated a prompt-based feature, which allows users to define a box around the target, outperforming the original nnU-Net model with a remarkably high DSC of 0.96 for HR-CTV and 0.91 for the rectum. All three studies found no statistically significant dosimetric differences between the manual and generated contours. These findings support the incorporation of a prompt-based feature in segmentation models to improve the results of complex structure segmentation, like the HR-CTV.

2.2.2 Prostate

For prostate brachytherapy, the target is typically visualized using PET/CT, TRUS, MRI, or CT during different procedures. Several studies have employed deep learning to segment the prostate, lesion, and OARs across different imaging modalities.

Dose boost on the dominant intraprostatic lesion (DIL) could potentially enhance the treatment outcomes [37, 121, 127]. Accurately segmenting the DIL is thus important for an effective DIL boost in prostate HDR brachytherapy plans, to ensure precise delivery of boost dose. PET/CT imaging can provide detailed morphological/anatomical information about the prostate and DIL. Matkovic et al. [78] used the Cascaded Regional-Net to automatically segment the prostate and DIL on PET/CT images. The Cascaded Regional-Net used a Dual Attention Network to extract deep features and identify the volume-of-interest (VOI) of the prostate, narrowing the location range of the DIL. Subsequently, a mask scoring regional convolutional neural network (MSR-CNN) detected the VOIs of the DILs and segmented the DIL from the prostate VOI. The MSDs were 0.666 ± 0.696 mm and 0.814 ± 1.002 mm, with DSCs of 0.932 ± 0.059 and 0.801 ± 0.178 for the prostate and DIL, respectively. The DSC for DIL is relatively low due to its small size and irregular shape. The CT scans provide additional anatomical structures of the patient but may add complexity in lesion segmentation. Wang et al. [126] conducted a similar study using Cascaded U-net to segment the lesions on PET scans with and without CT information. More lesions were detected on PET only compared to PET/CT scans (153/155 vs. 144/155), but there was no statistically significant difference in the DSC and HD95 between the PET only and PET/CT images as indicated in Table 3. Additionally, other studies investigated lesion segmentation using different methods. Li et al. [69] tested their model on 56 PET/CT scans from external institutions and showed no statistically significant difference compared to the internal testing results.

Prostate brachytherapy relies on TRUS images to guide implants. Accurate delineation of the prostate and OARs may enable a TRUS-based planning workflow, eliminating the need for additional CT or MR scans. However, as illustrated in Figure 5, the segmentation process is challenging due to the unclear

TABLE II. AI-based GYN-related segmentation results

Image Modality	Number of Patients	Model	Evaluation Parameters	Results						Citation
				HR-CTV	Bladder	Rectum	Sigmoid Colon	Small Intestine	GTV	
MRI	39	ResNet50 and InRN	DSC	0.85 ± 0.06	0.90 ± 0.05	0.76 ± 0.07	0.65 ± 0.12	0.54 ± 0.12	0.62 ± 0.14	[135]
			HD95 (mm)	4.87 ± 2.19	6.28 ± 3.42	8.20 ± 4.07	20.44 ± 11.70	22.3 ± 13.66	6.83 ± 2.89	
MRI	129 for MR1 and 52 for MR2	3D Dense U-Net	DSC (MR1)	-	0.93 ± 0.04	0.87 ± 0.03	0.80 ± 0.10	-	-	[140]
			DSC (MR2)	-	0.94 ± 0.05	0.88 ± 0.04	0.80 ± 0.05	-	-	
			HD95 (mm) (MR1)	-	4.18 ± 0.52	2.54 ± 0.41	5.03 ± 1.31	-	-	
			HD95 (mm) (MR2)	-	2.89 ± 0.33	2.24 ± 0.40	3.28 ± 1.08	-	-	
MRI	136	nnU-Net and transfer learning	vDSC	-	0.93 ± 0.04	0.87 ± 0.06	0.7 ± 0.2	0.7 ± 0.1	-	[82]
			(US)	-	-	-	-	-	-	
			sDSC	-	0.80 ± 0.07	0.78 ± 0.09	0.7 ± 0.1	0.5 ± 0.1	-	
			(US)	-	-	-	-	-	-	
			HD95 (mm)	-	4 ± 5	7 ± 5	20 ± 15	20 ± 15	-	
			(US)	-	-	-	-	-	-	
			vDSC	-	0.93 ± 0.04	0.85 ± 0.06	0.7 ± 0.1	0.7 ± 0.3	-	
			(UA)	-	-	-	-	-	-	
			sDSC	-	0.76 ± 0.07	0.70 ± 0.08	0.6 ± 0.1	0.5 ± 0.2	-	
			(UA)	-	-	-	-	-	-	
			HD95 (mm)	-	4 ± 2	10 ± 8	20 ± 15	30 ± 30	-	
			(UA)	-	-	-	-	-	-	
MRI	121	DCT-UNet	DSC (T2SPACE)	0.70 ± 0.12	0.94 ± 0.10	0.92 ± 0.11	0.84 ± 0.15	-	-	[61]
			DSC (T2QM)	0.66 ± 0.10	0.98 ± 0.02	0.81 ± 0.04	0.80 ± 0.09	-	-	
MRI	195	3D nnU-Net	DSC	-	-	-	-	-	0.73 [0.50-0.80]	[101]
			HD95 (mm)	-	-	-	-	-	6.8 [4.2-12.5]	
			MSD (mm)	-	-	-	-	-	1.4 [0.9-2.8]	
MRI	125	3D U-Net	DSC	0.85 ± 0.03	-	-	-	-	-	[141]
			HD95 (mm)	3.70 ± 0.35	-	-	-	-	-	
MRI and CT	65	Dual-path CNN	DSC	0.76 ± 0.06	-	-	-	-	-	[11]
			HD95 (mm)	5.99 ± 1.68	-	-	-	-	-	
			Sensitivity	0.81 ± 0.04	-	-	-	-	-	
			Precision	0.83 ± 0.04	-	-	-	-	-	
CT	91	DSD-UNET	DSC	0.83 ± 0.04	0.87 ± 0.03	0.82 ± 0.05	0.65 ± 0.08	0.80 ± 0.06	-	[146]
			HD (mm)	8.1 ± 2.3	12.1 ± 4.0	9.2 ± 4.6	19.6 ± 8.7	27.8 ± 10.8	-	
			Jaccard Index	0.72 ± 0.04	0.78 ± 0.03	0.72 ± 0.05	0.52 ± 0.08	0.69 ± 0.06	-	
CT	200	RefineNet	DSC	0.861	0.86	0.858	0.664	0.563	-	[56]
			HD (mm)	6.005	19.98	12.27	98.41	68.12	-	
			Overlap Index	0.839	0.783	0.894	0.601	0.811	-	
CT	62	nnU-Net	DSC	0.84 ± 0.07	0.94 ± 0.05	0.83 ± 0.07	-	-	-	[70]
			HD95 (mm)	7.42 ± 5.02	3.50 ± 1.96	7.58 ± 5.86	-	-	-	
			MSD (mm)	2.09 ± 1.31	0.94 ± 0.50	3.60 ± 3.49	-	-	-	
CT	100	nnU-Net	DSC	0.81 ± 0.05	0.92 ± 0.04	0.84 ± 0.04	-	-	-	[25]
			HD95 (mm)	6.03 ± 2.01	3.00 ± 1.09	5.25 ± 1.78	-	-	-	
			MSD (mm)	2.23 ± 0.75	0.84 ± 0.30	1.36 ± 0.43	-	-	-	
			Precision	0.80	0.91	0.84	-	-	-	
CT	60	Modified CNN	DSC	0.87	0.94	0.86	0.79	0.92	-	[124]
			HD95 (mm)	1.45	4.52	2.52	10.92	8.83	-	
CT	98	SEResU-Net	DSC	0.81 ± 0.05	0.92 ± 0.03	0.85 ± 0.05	0.60 ± 0.12	0.83 ± 0.09	-	[153]
			HD95 (mm)	5.23 ± 1.39	4.75 ± 1.48	4.06 ± 1.68	30 ± 8.16	20.5 ± 9.88	-	
CT	321	Prompt-nnUnet	DSC	0.96 ± 0.02	-	0.91 ± 0.02	-	-	-	[133]
			HD95 (mm)	1.66 ± 1.11	-	3.07 ± 0.94	-	-	-	
			IoU	0.92 ± 0.04	-	0.84 ± 0.03	-	-	-	
CT	113	ResU-Net	DSC	-	0.96 ± 0.04	0.97 ± 0.02	0.92 ± 0.03	-	-	[79]
			HD (mm)	-	4.05 ± 5.17	1.96 ± 2.19	3.15 ± 2.03	-	-	
			MSD (mm)	-	1.04 ± 0.97	0.45 ± 0.09	0.79 ± 0.25	-	-	
CT	51	3D U-Net and Long Short-Term Memory	DSC	0.87 ± 0.063	0.86 ± 0.049	0.77 ± 0.084	0.73 ± 0.0102	-	0.72 ± 0.091	[12]
			sDSC	0.81 ± 0.007	-	-	-	-	-	
			vDSC	0.88 ± 0.001	-	-	-	-	-	
			Surface Overlap	0.78 ± 0.007	-	-	-	-	-	[50]
			HD (mm)	3.20 ± 2.00	-	-	-	-	-	
			MSD (mm)	0.69 ± 0.06	-	-	-	-	-	

Note: Abbreviations: US (unseen scanner), UA (unseen applicator), vDSC (volumetric dice similarity coefficient), sDSC (surface dice similarity coefficient), DSD-UNET (dilated convolution and deep supervision U-Net), SEResU-Net (U-Net with squeeze-and-excitation ResNet), IoU (intersection over union), Mnet_IM (improved M-Net model).

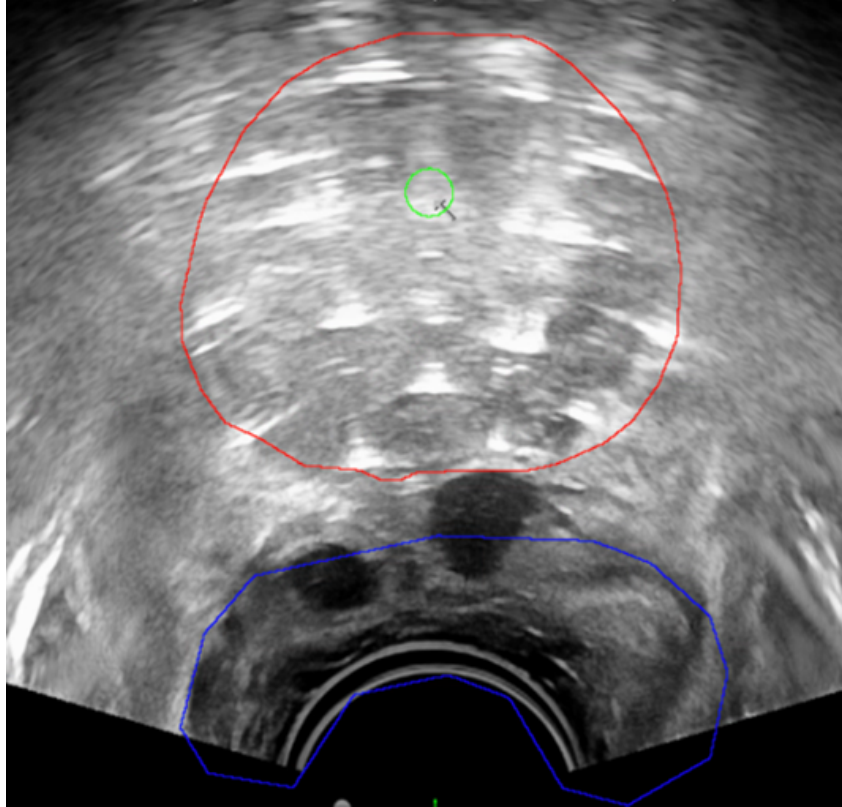


Figure 5: Example of organ segmentation on TRUS used in prostate brachytherapy. Red: prostate; blue: rectum; green: urethra.

boundary between the prostate and rectum, making it highly dependent on the clinician' experience.

Several studies have successfully used different deep-learning models to segment the prostate on TRUS images, and the detailed results are summarized in Table 3 [7, 33, 34, 40, 60, 65, 86, 91, 132, 144]. Among these studies, the most accurate contours are reported from the semi-automatic models by Girum et al. [34] and Peng et al. [91], both of which achieved DSCs of more than 0.96 for the prostate segmentation. Girum et al. used a weakly supervised deep learning method, which is a fully connected CNN with a prior knowledge generator block and a segmentation block. The weakly supervised method is more effective and less time-consuming than training with fully labeled image data. The segmentation highly accurate DSC of 0.969 ± 0.009 and HD of 4.25 ± 4.58 mm on TRUS. Interestingly, this model can also be directly implemented on CT, despite being trained on TRUS images, with only slightly inferior results (DSC = 0.954 ± 0.009 and HD = 5.17 ± 1.41 mm). This study showed the potential for model adaptation between different imaging modalities, which enables the model to be implemented in imaging modalities with limited data. Peng et al. built an A-ProSeg model, which combines a closed-principle-curve-based method, a global closed polygonal segment method, and memory-based differential evolution model to identify prostate vertices and create a smooth prostate contour. The model demonstrated robustness as was trained and tested on a diverse dataset containing 226 patients with 945 TRUS slices in total. It achieved a DSC of 0.962 ± 0.024 and a HD of 1.9 ± 0.9 mm and maintained a similar segmentation performance even when the TRUS images were set to a low signal-to-noise ratio (SNR) of 0.8. It is worth to note that both methods were semi-automatic, requiring pseudo-landmarks or radiologist-defined points as inputs, which may be prone to user errors or inter-observer variability.

Fully automatic models can further simplify the contouring process as they do not require human intervention. Orlando et al. [87] trained and validated an accurate fully automatic model for segmenting the prostate on TRUS on a large dataset of 246 patients. A 2D modified U-Net was built to predict the 2D radial slices from TRUS images and the predicted prostate slices were reconstructed in 3D. Using this configuration, the median DSC was 0.94, HD was 2.89 mm, volume percent differences (VPD) was 5.78%, and MSD was 0.89 mm. This group conducted another study comparing U-Net and U-Net++ with different training configurations. [88] The U-Net++ model achieved the most optimal segmentation performance with a training dataset size of 1,000 2D images, regardless of the imaging acquisition

TABLE III

Image Modality	Number of Patients	Model	Evaluation Parameters	Results						Citation		
				Prostate	Prostate Lesion	Bladder	Rectum	Urethra	Seminal Vesicles			
PET/CT	49	Cascaded Regional Net and MSR-CNN	DSC	0.932 ± 0.059	0.801 ± 0.178	-	-	-	-	[78]		
PET/CT	84	U-net, Cascaded U-net, and cascaded detection segmentation network	MSD (mm)	0.666 ± 0.696	0.814 ± 1.002	-	-	-	-	-	[126]	
			DSC (PET/CT)	-	0.68 ± 0.15	-	-	-	-	-		-
			DSC (PET only)	-	0.68 ± 0.17	-	-	-	-	-		-
			HD95 (mm) (PET/CT)	-	3.98 ± 2.23	-	-	-	-	-		-
			HD95 (mm) (PET only)	-	4.16 ± 2.33	-	-	-	-	-		-
PET/CT	137	UNETR	Detection rate (PET/CT)	-	144/155	-	-	-	-	-	[69]	
			Detection rate (PET only)	-	153/155	-	-	-	-	-		-
			DSC (internal)	-	0.70	-	-	-	-	-		-
			DSC (external)	-	0.68	-	-	-	-	-		-
			IoU (internal)	-	0.566	-	-	-	-	-		-
			IoU (external)	-	0.548	-	-	-	-	-		-
			Precision (internal)	-	0.809	-	-	-	-	-		-
			Precision (external)	-	0.749	-	-	-	-	-		-
			Recall (internal)	-	0.66	-	-	-	-	-		-
			Recall (external)	-	0.74	-	-	-	-	-		-
TRUS and CT	145	Weakly-supervised CNN and unsupervised CNN	DSC (TRUS)	0.969 ± 0.009	-	-	-	-	-	-	[34]	
			DSC (CT)	0.954 ± 0.009	-	-	-	-	-	-		
			3D HD (mm) (TRUS)	4.25 ± 4.58	-	-	-	-	-	-		
			3D HD (mm) (CT)	5.17 ± 1.41	-	-	-	-	-	-		
			Volumetric Overlap Ratio (TRUS)	0.939 ± 0.180	-	-	-	-	-	-		
TRUS	226	A-ProSeg	Volumetric Overlap Ratio (CT)	0.913 ± 0.170	-	-	-	-	-	[91]		
			DSC	0.962 ± 0.024	-	-	-	-	-		-	
TRUS	246	2D modified U-Net and 3D reconstruction	JI	0.944 ± 0.033	-	-	-	-	-	-	[87]	
			Accuracy	95.7 ± 2.7%	-	-	-	-	-	-		-
			DSC	0.941 [0.926, 0.949]	-	-	-	-	-	-		-
			Precision	93.2 [88.8, 95.4] %	-	-	-	-	-	-		-
			Recall	96.0 [93.1, 98.5] %	-	-	-	-	-	-		-
TRUS	44	Multidirectional Deeply Supervised V-Net	VPD	5.78 [2.49, 11.50] %	-	-	-	-	-	-	[65]	
			HD (mm)	2.89 [2.37, 4.35]	-	-	-	-	-	-		
			MSD (mm)	0.89 [0.73, 1.09]	-	-	-	-	-	-		
			DSC	0.92 ± 0.03	-	-	-	-	-	-		
TRUS	675	CNN	HD (mm)	3.94 ± 1.55	-	-	-	-	-	[60]		
			MSD (mm)	0.60 ± 0.23	-	-	-	-	-		-	
TRUS	145	Encoder-decoder CNN and DNN	DSC	0.939 ± 0.035	-	-	-	-	-	[33]		
			HD (mm)	2.7 ± 2.3	-	-	-	-	-		-	
			DSC	0.88 ± 0.02	-	-	-	-	-		-	
TRUS	598	ResU-Net	HD95 (mm)	2.01 ± 0.54	-	-	-	-	-	[71]		
			Accuracy	96 ± 1%	-	-	-	-	-		-	
TRUS	590	Multi-label method with K-SVD	MSD (mm)	0.1 ± 0.06	-	-	-	-	-	-	[86]	
			DSC	0.937 ± 0.037	-	-	-	-	-	-		
			HD (mm)	3.0 ± 2.05	-	-	-	-	-	-		
			MSD (mm)	1.05 ± 0.71	-	-	-	-	-	-		
			Volumetric Error (CTV)	9.95 ± 3.53%	-	-	-	-	-	-		
TRUS	315	PTN and CPTTA	Volumetric Error (PTV)	8.84 ± 3.13%	-	-	-	-	-	-	[132]	
			HD (mm) (CTV)	5.40 ± 1.38	-	-	-	-	-	-		
			HD (mm) (PTV)	5.48 ± 1.51	-	-	-	-	-	-		
			MSD (mm) (CTV)	0.98 ± 0.39	-	-	-	-	-	-		
			MSD (mm) (PTV)	1.19 ± 0.48	-	-	-	-	-	-		
TRUS	132	2D U-Net CNN	DSC	0.899 ± 0.035	-	-	-	-	-	[40]		
			HD (mm)	7.07 ± 3.19	-	-	-	-	-		-	
			MSD (mm)	1.30 ± 0.61	-	-	-	-	-		-	
TRUS and MRI	598	End-to-end CNN	DSC	0.872 [0.841, 0.888]	-	-	-	-	-	[144]		
			HD (mm)	6.0 [5.3, 8.0]	-	-	-	-	-		-	
			MSD (mm)	1.6 [1.2, 2.0]	-	-	-	-	-		-	
TRUS	83	Anchor-free mask CNN	DSC	0.909 ± 0.022	-	-	-	-	-	[68]		
			DSC (cross validation)	0.95 ± 0.03	-	0.75 ± 0.012	0.90 ± 0.07	0.86 ± 0.07	-		-	
			DSC (hold-out)	0.94 ± 0.03	-	0.76 ± 0.13	0.92 ± 0.03	0.85 ± 0.06	-		-	
			HD (mm) (cross validation)	2.28 ± 0.64	-	2.58 ± 0.7	1.65 ± 0.52	1.85 ± 1.71	-		-	
			HD (mm) (hold-out)	2.27 ± 0.79	-	2.93 ± 1.29	1.90 ± 0.28	1.81 ± 0.72	-		-	
MRI	200	2D and 3D U-Net FCNs	DSC (T2)	0.90 ± 0.04	-	0.96 ± 0.04	0.91 ± 0.06	-	0.80 ± 0.12	[105]		
			DSC (T1)	0.82 ± 0.07	-	0.88 ± 0.05	0.87 ± 0.06	-	0.46 ± 0.21			
CT	215	DLAS	DSC (re-trained)	0.82	-	0.92	-	-	0.48	[23]		
DSC (built-in)	0.73	-	0.81	-	0.37	-	-					

Note: Abbreviations: DNN (deep neural network), PTN (polar transform network), CPTTA (centroid perturbed test-time augmentation), K-SVD (K-singular value decomposition), A-ProSeg (accurate prostate segmentation framework).

type (end-fire, side-fire, or mixed). Interestingly, increasing the training data size does not significantly enhance the segmentation results but add additional training time.

In prostate brachytherapy, the OARs include the rectum, bladder, and seminal vesicles due to their proximity to the prostate. An efficient and accurate segmentation method of these organs is essential to minimize unnecessary radiation dose and reduce treatment toxicity. Three groups have provided methods to segment the prostate and OARs on TRUS, MRI, or CT images.

Lei et al. [68] designed an anchor-free mask CNN that utilized a fully convolutional one-state object detector that simultaneously segment the prostate, bladder, rectum, and urethra on 3D TRUS images within 5 seconds per patient. This model provides fast segmentation on all organs but has limitations in the segmentation accuracy of the bladder, constrained by the low contrast on ultrasound images. Sanders et al. [105] trained 120 models with different combinations of 18 FCNs and different convolutional encoders, to segment the prostate and the OARs in T1, T2/T1, and T2-weighted MRIs. Among all combinations, an FCN with a DenseNet201 encoder yielded the most optimal results besides the external urinary sphincter and the seminal vesicles, due to their complex shapes. While the model was trained exclusively on T2-weighted and T2/T1-weighted contrast images, it can also be transferred to T1-weighted MRI with slightly reduced accuracy. Duan et al. [23] conducted a study to assess the efficacy of the commercial deep learning auto-segmentation (DLAS) software in automatically segmenting the male pelvis on CT scans. Retraining the DLAS software with institutional data, the segmentation results improved for the prostate and OARs compared to the built-in setup.

2.3 Other Imaging Applications

In addition to aiding with image registration and segmentation, AI can enhance medical image quality and generate synthetic images to improve diagnosis and other steps in the brachytherapy workflow.

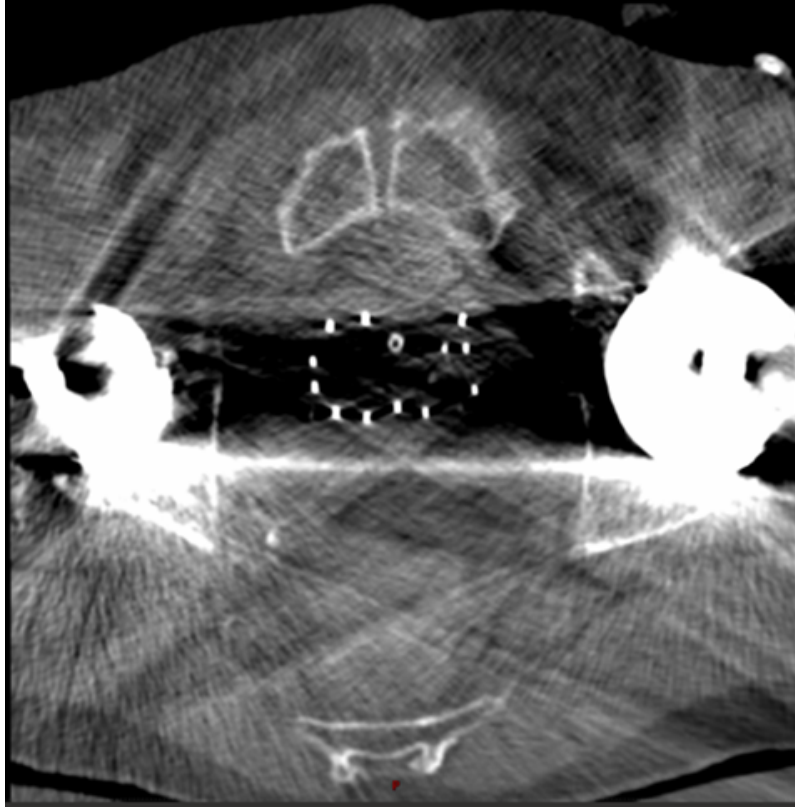


Figure 6. Example of metal artifacts caused by hip prosthesis in a CT scan for prostate brachytherapy.

These applications are presented in Table 4.

Metal artifacts on CT images may complicate organ and applicator visualization. Figure 6 is an example of how metal artifacts caused by hip prosthesis can complicate the visualization of patient anatomy and applicators on CT scans. Huang et al. [51] built a residual learning method based on CNN (RL-ARCNN) to reduce metal artifacts on CT images for GYN cancer brachytherapy. They generated 600 simulated artifact image slices from 20 GYN cancer patients to train and validate the RL-ARCNN model. Using residual learning, the peak signal-to-noise ratio (PSNR) was the highest among all different image patch sizes with the best result of 38.09 dB in 50 by 50 patch size.

Photoacoustic imaging, used for detecting prostate low-dose-rate (LDR) brachytherapy seeds, is susceptible to acoustic wave reflection artifacts. Allman et al. [6] built a CNN to identify artifacts and true source (LDR seeds), and reduce the reflection artifact created by photoacoustic waves to improve the quality of seed reconstruction. The CNN model achieved a low localization error of point source with mean \pm SD of 0.40 ± 0.22 mm and 0.38 ± 0.25 mm, and a high classification accuracy of 100

Deep learning can also improve image quality by increasing resolution. In practice, 3D TRUS images with low resolution are usually captured with thick slice of (2-5 mm) in brachytherapy due to time constraint. He et al. [43] developed a GAN-based framework integrated with a deeply supervised attention model to construct high-resolution ultrasound images from the low-resolution TRUS images. The model was trained with high and low-resolution TRUS image pairs from 20 patients, with the high-resolution images served as ground truths. The proposed model achieved a mean absolute error (MAE) of 6.5 ± 0.5 and a high PSNR of 38.0 ± 2.4 dB.

In addition to enhancing image resolution, deep learning models can also synthesize images, such as generating synthetic MRI from CT images, combining the cost efficiency of CT with the soft tissue contrast of MRI. Podgorsak et al. [95] and Kang et al. [59] both utilized Pix2Pix [54] and CycleGAN to build DL-based models to create synthetic MRI from CT scans, namely PCGAN and PxCGAN. Both studies evaluated the quality of the synthetic MRIs by comparing contour differences between real and synthetic MRIs within the same radiation oncologist (inter-modality) and segmentation differences among different radiation oncologists within the same image (inter-observer). As presented in Table 4, both studies successfully visualized the prostate and catheters on the synthetic MRIs and showed that the

TABLE IV. AI implementation on other imaging applications

Application	Cancer Site	Image Modality	Number of Patients	Model	Result Summary	Citation
Reduce metal artifacts	GYN	CT	35	RL-ARCNN	PSNR = 33.83 dB, 38.09 dB, and 36.80 dB for 25 by 25, 50 by 50, and 100 by 100 image patch sizes respectively.	[51]
Remove artifacts	Prostate	Photoacoustic	17,340 images	CNN	From the water bath and phantom test, the mean localization error of point source were 0.40 ± 0.22 mm and 0.38 ± 0.25 mm.	[6]
Improve resolution	Prostate	TRUS	20	GAN and Attention	Mean MAE for reconstructed images = 6.5 ± 0.5 and PSNR = 38.0 ± 2.4 dB.	[43]
Synthetic MRI from CT	Prostate	CT - MRI	78	PCGAN	DSC = 0.852 ± 0.057 and MSD = 2.47 ± 0.50 mm for interobserver contour differences; DSC = 0.846 ± 0.045 and MSD = 2.19 ± 0.69 mm for intermodality contour differences.	[95]
Synthetic MRI from CT	Prostate	CT - MRI	78	PxCGAN	DSC = 0.84 ± 0.05 , MSD = 2.30 ± 0.67 mm, and HD = 10.11 ± 2.71 mm for interobserver contour differences; DSC = 0.84 ± 0.05 , MSD = 2.19 ± 0.69 mm, and HD = 8.34 ± 2.27 mm for intermodality contour differences. MAE = 0.14 ± 0.03 , MSE = 0.04 ± 0.01 , PSNR = 68.69 ± 1.44 dB, and structural similarity index (SSIM) = 0.73 ± 0.11 for differences between synthetic MRI and real MRI.	[59]
Synthetic MRI from CT	Prostate	CT - MRI	140	CycleGAN and deep attention U-Net	For synthetic MRI generated segmentations: DSC = 0.95 ± 0.03 and MSD = 0.52 ± 0.22 mm for bladder, DSC = 0.87 ± 0.04 and MSD = 0.93 ± 0.51 mm for the prostate, DSC = 0.89 ± 0.04 and MSD = 0.92 ± 1.03 mm for the rectum.	[22]
Synthetic MRI from CT	Prostate	CT - MRI	49	CycleGAN	For synthetic MRI generated segmentations: DSC = 0.92 ± 0.09 , HD = 4.38 ± 4.66 mm, and MSD = 0.62 ± 0.89 mm for the leave-one-out test. DSC = 0.91 ± 0.07 , HD = 4.57 ± 3.03 mm, and MSD = 0.62 ± 0.65 mm for the hold-out test.	[67]

DSC and MSD from inter-modality contours are comparable or better than the inter-observer differences. However, the limited patient dataset used in these studies may impact the generalizability of the models, which affect the image quality and corresponding dosimetric parameters on new synthetic MRIs. For instance, the dosimetric parameters for PTV and OARs from the synthetic MRI were generally higher than those from the actual MRI but had no statistically significant difference except for bladder D_{1cc} , potentially caused by the effect of catheter position on the target. Overall, this approach has the potential to improve clinical workflows by reducing the need for additional MRI scans.

3 Preplanning

The preplanning process involves developing a brachytherapy treatment plan outside the operating room prior to its delivery to the patient. As summarized in Table 5, this process can be applied to both GYN and prostate brachytherapy treatments.

3.1 GYN

For HDR GYN brachytherapy, preplanning involves selecting the appropriate applicators, either intracavitary (IC) or interstitial (IS), based on patient anatomy. Stenhouse et al. [113] trained 12 machine learning models to predict the use of IC or IS applicator for different GYN cancer patients, selecting the top three models for final predictions. Important features, such as the needle patterns and clinical contours, were selected by an F-test to reduce complexity introduced by unnecessary features. An AdaBoost Classifier, a Gradient Boosting Classifier, and a Random Forest (RF) Classifier were selected to form a voting model because of their superior performances. The final voting model, formulated from the weighted average of the predicted probabilities from the three models, provides applicator

decisions with an accuracy of $91.5 \pm 0.9\%$ and a F1 Score of $90.6 \pm 1.1\%$. Another important factor to consider when selecting the appropriate applicator is soft-tissue deformation caused by applicator insertion. Applicators used in GYN brachytherapy can induce an average point-to-point displacement of 25.0 mm in the uterus. [31] Knowing the changes in soft tissue location post-insertion gives physicians additional information for selecting the most effective applicator. Ghosh et al. [31] used a deep-learning model to automatically predict uterus deformation caused by applicators using only pre-surgery MRI as input. The model utilized a deep CNN model with auto-encoders for pre-surgery uterus segmentation and a modified U-Net for predicting the uterus deformation during implantation. The predicted new uterine position had a DSC of 0.881 ± 0.038 and an HD of 5.8 ± 3.6 mm compared to the true deformed position.

3.2 Prostate

In LDR prostate brachytherapy, preplanning involves determining the seed distribution and the resulting dose distribution prior to the treatment day. Manual planning is time-consuming and heavily dependent on the experience level of the planner. Nicolae et al. [85] built a machine learning-based prostate implant planning algorithm (PIPA) system to automate treatment planning for LDR prostate patients. The percentages of plans that need minor or major modification were approximately the same for PIPA and manual method, but the algorithm reduced the planning time to 2.38 ± 0.96 minutes compared to 43.13 ± 58.70 minutes. However, this model was only tested on a small cohort of 41 patients and did not report differences in dose-volume histogram (DVH). In 2021, Aleef et al. [3] employed a two-stage framework that consisted of conditional generative adversarial networks (cGAN) to automatically generate treatment plans. The cGAN model predicted needle distribution, and a simulated annealing algorithm optimized seed location. Overall, 90% of the generated treatment plans were acceptable, with 60% requiring minor modifications and 30% requiring major modifications. Additionally, significantly less time (3 minutes compared to 20 minutes) was required for an automatic plan with similar quality to manual plans (a CTV V_{100} value of 98.98% compared to 99.36%). In a later study [4], the researchers developed a treatment planning generative adversarial network (TP-GAN) and achieved similar DVH with less urethral doses in only 2.5 minutes or 3 seconds per plan with and without fine-tuning. Deep learning models are also potential substitutes for traditional computational models such as Monte Carlo (MC) simulations due to their fast-processing speed. Berumen et al. used a 3D U-Net based model that learns MC simulations to predict single-seed dose to medium ($D_{M,M}$) on CT images, which produced similar DVH metrics but in significantly less time than MC methods (1.8 ms compared to 2 hours).

In intraoperative LDR brachytherapy, extra seeds are usually ordered to ensure sufficient coverage. However, unused seeds in the procedure would require physicist to spend additional time documenting and safely returning them to the vendor. To address this, Boussion et al. [10] used several machine-learning models to predict the number of seeds needed for LDR prostate brachytherapy. The best-performing ML model, support vector machines for regression (SVR), reduced the unused seeds from 23 ± 4 to 10 ± 4 when tested on 38 unseen treatments, though a 10% margin is still necessary to prevent seed depletion during implant.

4 Treatment Planning

In HDR brachytherapy, both prostate and GYN, the treatment planning procedure is often performed intraoperatively with patients under anesthesia or immobilized, which makes it highly time sensitive. The detailed methods and results of recent studies employing AI to support the treatment planning process are summarized in Table 6.

4.1 Prostate

In HDR brachytherapy, the dose distribution largely depends on the positions of applicators, which vary per patient, making the dose prediction challenging. Figure 7 is an example of prostate HDR treatment

TABLE V. AI application in preplanning

Preplanning Task	Cancer Site	Number of Patients	Model	Result Summary	Citation
Select Applicator	GYN	233	AdaBoost, Gradient Boost, and RF classifier	Accuracy = $91.5 \pm 0.9\%$ and F1 Score = $90.6 \pm 1.1\%$.	[113]
Predict Applicator Induced Uterine Deformation	GYN	92	CNN and modified U-Net	For predicted uterine position after applicator insertion: DSC = 0.881 ± 0.038 and HD = 5.8 ± 3.6 mm.	[31]
Generate Preplans	Prostate	150	K-nearest neighbor	No significant difference in prostate V_{100} , prostate D_{90} , urethra $D_{0.1cc}$, rectum D_{1cc} , PTV $V_{100\%}$ between manual and ML plans, except prostate $V_{150\%}$ was 4% lower for ML plans.	[83]
Generate Preplans	Prostate	41	PIPA	No significant differences in prostate $D_{90\%}$, $V_{100\%}$, rectum $V_{100\%}$, or rectum D_{1cc} between manual and PIPA plans.	[84]
Predict Needles and Seeds Distribution	Prostate	931	cGAN	98.98% achieved 100% of the prescribed dose, 90% of the generated plans were acceptable with 60% minor and 30% major modifications. PTV $V_{100\%} = 96.55 \pm 1.44$, PTV $V_{150\%} = 56.23 \pm 4.37$, CTV $V_{100\%} = 99.36 \pm 0.96$, CTV $V_{150\%} = 63.03 \pm 5.15$.	[3]
Predict Seeds Distribution	Prostate	961	TP-GAN	98.98% achieved 100% of the prescribed dose. TPGAN only: PTV $V_{100\%} = 94.6 \pm 3.9$, PTV $V_{150\%} = 55.0 \pm 11.9$, CTV $V_{100\%} = 97.8 \pm 2.5$, CTV $V_{150\%} = 60.8 \pm 13.7$. TPGAN and Simulating Annealing: PTV $V_{100\%} = 95.9 \pm 1.6$, PTV $V_{150\%} = 53.0 \pm 3.5$, CTV $V_{100\%} = 98.8 \pm 0.9$, CTV $V_{150\%} = 59.1 \pm 5.0$.	[4]
Predict Single-Seed Dose to Medium in Medium	Prostate	44	3D U-Net CNN	The average differences of the predicted and MC-based calculations were 0.1% for CTV D_{90} and 1.3%, 0.07%, and 4.9% for the D_{2cc} of rectum, bladder, and the urethra.	[9]
Predict Number of Seeds	Prostate	409	SVR	MSE = 2.55, MAE = 1.21, and maximum error = 7.29 seeds. When tested on 38 unseen treatments, reduced unused seeds from 23 ± 4 to 10 ± 4 seeds, and saved 493 seeds in total.	[10]

Note: Abbreviations: MSE (mean squared error).

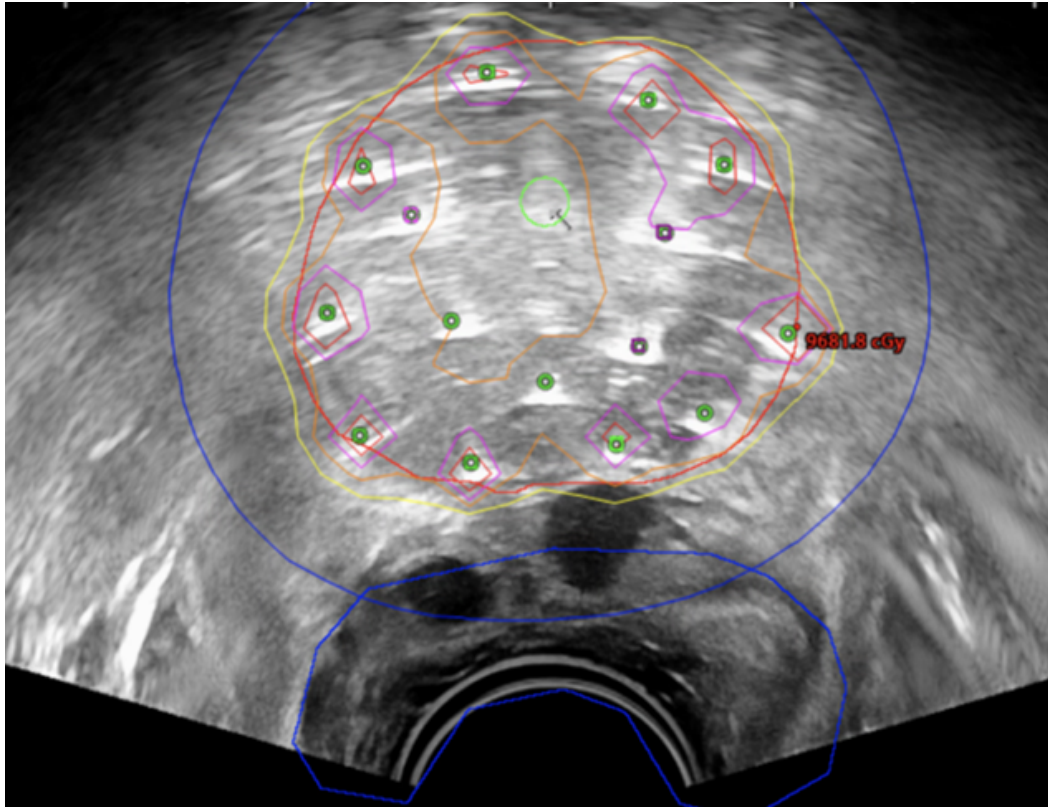


Figure 7. Example of HDR prostate brachytherapy treatment planning on TRUS.

planning performed intraoperatively on TRUS. AI can analyze large datasets and identify complex patterns, allowing it to predict DVH for the CTV and OARs. [2, 14, 18, 55, 71, 77, 122, 138, 147, 151]

Mao et al. [77] trained a 3D deep convolutional neural network (DCNN), RapidBrachyDL, to perform dose calculations based on the MC method. RapidBrachyDL had errors less than 1.5% for the CTV and OAR DVH metrics as shown in Table 6, comparable to the conventional MC method. Interestingly, although trained with prostate patient data only, it showed transferability to cervical cancer patient CT scans with errors below 3%. Similarly, Villa et al. [122] trained a DCNN model with MC-based method generated database, achieving fast inverse planning in only 1.7 seconds with small mean percent errors (MPE).

To guide the placement of catheters in HDR prostate brachytherapy, Lei et al. [66] developed Reg-Net, a 3D CNN based deformable multi-atlas registration network. Reg-Net used distance maps of targets and OARs to register with new patient CT images and predict catheter locations. The resulting DVH metrics from predicted catheter distributions differed by no more than 5% different from clinical plans, though there were hot spots in the prostate and excessive dose in OARs. This model quantifies dose distribution on CT simulations prior to catheter placements, locates catheters more effectively, which potentially reduces intuitive decision-making in the HDR procedures.

4.2 GYN

For HDR GYN brachytherapy, knowledge-based planning (KBP) using traditional methods has been proven to standardize treatment plans and effectively predict dose volumes by learning the correlation between the final plan dosimetry and patient-specific characteristics [139]. KBP uses spatial information of patient anatomy and applicators to predict 3D dose for high-quality treatment plans. Cortes et al. [18] applied a 3D U-Net CNN to conduct KBP for HDR cervical cancer brachytherapy using tandem and ovoids (T&O) applicators. This model provided objective dose measures for HR-CTV D_{90} and OAR D_{2cc} , potentially offering quality checks for planners. MC-based dose calculation can also be performed with DL models. Akhavanallaf et al. [2] developed a deep neural network (DNN)-based model, personalized brachytherapy dosimetry simulator (PBrDoseSim), to calculate dose with the MC method.

PBrDoseSim predicted the specific energy deposition kernel when the radioactive source is positioned at the dwell position, which exhibited good agreement with MC calculations. Additionally, the study provided a baseline comparison and an evaluation of their full dose distribution against the ground truth as shown in Table 6. The study is limited by using the contours instead of the direct density maps from the CT images.

To increase model robustness against different GYN brachytherapy settings, Li et al. [71] trained a Squeeze and Excitation Attention Net (SE_{AN}) with various clinically common applicators including vaginal applicator, ovoid applicator, T&O applicators, free needles, and multi-channel applicator. The smallest MAE of the predicted DVH metrics from SE_{AN} , U-Net, and 3D Cascaded U-Net were summarized in Table 6. While SE_{AN} did not outperform U-Net and Cascaded U-Net in rectum and HRCTV MAEs, it predicted the correct number and dose gradient for each applicator setup and closely resembled the ground truth and had the highest gamma passing rate of 92 ± 10

Several studies showed AI model’s capability in predicting OAR dose [14, 55, 147, 151]. Two studies [14?] predicted the rectal toxicity levels from treatment plans, where the best sensitivity, or recall, is 84.75%, and the best specificity, or precision, is 79.87%. When using statistically significant features only, the model achieved an area under the receiver operating characteristic curve (AUC) of 0.91, indicating its strong discriminative ability. Zhang et al. [147] predicted the dose in bladder, rectum, and sigmoid using neural networks, correlating D_{2cm^3}/D_{90} for each OAR and its sub-organ, showing strong correlation and small mean squared error (MSE). Additionally, this model only requires sub-organ volumes of the OAR without additional voxel information, allowing physicians without programming experience to perform dose predictions.

Besides dose prediction, AI has several other applications in enhancing the treatment planning of HDR brachytherapy. For example, Gao et al. [30] used dose prediction network (DPN) and a plan-approval probability network (PPN) to predict the HDR plan approval probability. Pu et al. [96] provided a method, the intelligent treatment planner network (ITPN) to automatically adjust HDR source dwell times, optimizing until the objective function converges. Compared to a common clinical model, inverse planning simulated annealing (IPSA), the ITPN model preserved OARs better, notably reducing the bladder D_{2cc} , rectum V_{150} , sigmoid V_{150} , rectum V_{200} , and sigmoid V_{200} . Shen et al. [110] used deep reinforced learning-based optimization to provide automatic weight tuning in inverse treatment planning. The method consisted of a Weight Tuning Policy Network (WTPN) which automatically adjust the weights of OARs to produce high-quality plans, showing proficiency even trained on a limited dataset and potential for integration into other treatment planning optimization.

TABLE VI. AI application in treatment planning

Treatment Planning Task	Cancer Site	Number of Patients	Model	Results	Citation
Inverse Planning	Prostate	273	DCNN	For prostate: MPE = $-0.8 \pm 1.0\%$ for V_{100} , $-0.6 \pm 3.1\%$ for V_{150} , and $0.2 \pm 1.3\%$ for V_{200} . For OARs: MPE = $1.7 \pm 3.5\%$ for urethra D_{10} , $0.9 \pm 2.7\%$ for urethra D_{30} ; $0.4 \pm 2.6\%$ for rectum D_{2cc} , $2.8 \pm 9.2\%$ for rectum $D_{0.1cc}$.	[122]
Predict Catheter Placements	Prostate	90	Reg-Net	The difference between the clinical and predicted prostate V_{150} , V_{200} , and D_{90} were $5.0 \pm 6.5\%$, $2.9 \pm 4.3\%$, $0.9 \pm 1.5\%$, bladder D_{2cc} , V_{75} were $3.5 \pm 3.4\%$ and 0.2 ± 0.4 cc, rectum D_{2cc} , V_{75} were $1.5 \pm 4.1\%$ and 0.1 ± 0.4 cc, urethra V_{125} = 0.3 ± 0.4 cc.	[66]
CTV and OAR dose prediction	Prostate/GYN	61	RapidBrachyDL	For prostate cancer: dose prediction errors = 0.73%, 1.1%, 1.45%, 1.05%, for CTV D_{90} , rectum D_{2cc} , urethra $D_{0.1cc}$, and bladder D_{2cc} ; For cervical cancer: dose prediction errors = 1.73%, 2.46%, 1.68%, and 1.74% for CTV D_{90} , rectum D_{2cc} , sigmoid D_{2cc} , and bladder D_{2cc} , respectively.	[77]

CTV and OAR dose prediction	GYN	126	3D U-Net CNN	Isodose DSC = [0.87, 0.94], mean difference of the DVH metrics were -0.09 ± 0.67 Gy for HRCTV D_{90} , -0.17 ± 0.67 Gy for bladder D_{2cc} , -0.04 ± 0.46 Gy for rectum D_{2cc} , and 0.00 ± 0.44 Gy for sigmoid D_{2cc} .	[18]
CTV and OAR dose prediction	GYN	78	PBrDoseSim	For model predicted single-dwell dose kernels, MRAE = $1.16 \pm 0.42\%$ MAE = $4.2 \pm 2.7 \times 10^{-4}$ ($Gy \cdot sec^{-1}/voxel$). Conformity index = 0.24, dose non-uniformity ratio = 0.65, and dose homogeneity index = 0.34. The MRAE for CTV between DNN and MC were $1.5 \pm 0.88\%$ for D_{95} , $1.8 \pm 0.86\%$ for D_{90} , $1.3 \pm 1\%$ for D_{50} , $0.85 \pm 0.43\%$ for V_{200} , $0.56 \pm 0.56\%$ for V_{150} , $1.48 \pm 0.72\%$ for V_{100} , $0.26 \pm 0.38\%$ for V_{50} . The MRAE for OARs were $2.7 \pm 1.7\%$ and for bladder D_{5cc} and D_{2cc} , $1.9 \pm 1.3\%$ and $2.4 \pm 1.6\%$ for sigmoid D_{5cc} and D_{2cc} , and $2.1 \pm 1.7\%$ and $2.5 \pm 2\%$ for rectum D_{5cc} and D_{2cc} .	[2]
CTV and OAR dose prediction	GYN	81	SEAN	SEAN: MAE = 0.37 ± 0.25 for HRCTV D_{90} , 0.23 ± 0.14 for bladder D_{2cc} , 0.28 ± 0.20 for rectum D_{2cc} . U-Net: MAE = 0.34 ± 0.24 for HRCTV D_{90} , 0.25 ± 0.20 for bladder D_{2cc} , 0.25 ± 0.21 for rectum D_{2cc} . Cascaded U-Net: MAE = 0.42 ± 0.31 for HRCTV D_{90} , 0.24 ± 0.19 for bladder D_{2cc} , 0.23 ± 0.19 for rectum D_{2cc} .	[71]
CTV and OAR dose prediction	GYN	224	3D mask-guided dose prediction model	Dose prediction errors = 0.63 ± 0.63 , 0.60 ± 0.61 , 0.53 ± 0.61 , 1.21 ± 0.85 , 0.71 ± 0.61 , 1.16 ± 1.09 , and 0.86 ± 0.58 , for HRCTV D_{95} , HRCTV D_{95} , HRCTV D_{100} , bladder D_{2cc} , sigmoid D_{2cc} , rectum D_{2cc} , and intestine D_{2cc} .	[138]
Rectum dose prediction	GYN	42	VGG-16 and RSDM	10-fold cross validation: sensitivity = 61.1%, specificity = 70%, and AUC = 0.7. leave-one-out cross validation: sensitivity = 75% specificity = 83.3%, and AUC = 0.89.	[151]
Rectum dose prediction	GYN	42	SVM	Using principal component analysis (PCA) features: sensitivity = 74.75%, specificity = 72.67%, and AUC = 0.82; Using statistically significant features: sensitivity = 84.75%, specificity = 79.87%, and AUC = 0.91.	[14]
OAR dose prediction	GYN	59	LM algorithm	R= 0.80 for bladder, 0.88 for rectum, and 0.86 for sigmoid; MSE = 5.543×10^{-3} for bladder D_{2cc}/D_{90} , 5.028×10^{-3} for rectum D_{2cc}/D_{90} , and 8.815×10^{-3} for sigmoid D_{2cc}/D_{90} .	[147]
Predict Plan Approval Probability	GYN	63	DPN and PPN	Dose prediction error = $11.51\% \pm 6.92\%$ for bladder, $8.23\% \pm 5.75\%$ for rectum, $7.12\% \pm 6.00\%$ for sigmoid D_{2cc} , and $10.16\% \pm 10.42\%$ for CTV D_{90} . Plan approval prediction: accuracy = 0.70, sensitivity = 0.74, specificity = 0.65, and AUC = 0.74.	[30]
Inverse planning - dwell times	GYN	20	ITPN	Directly output the dwell times of pre-selected dwell positions of HDR BT for cervical cancer, generate higher quality plans with better CTV coverage and OARs sparing compared to clinically accepted IPSA.	[96]

Organ Weighting Factor Adjustment	GYN	10	WTPN	Plan quality score was improved by 8.5% compared to the initial plan with arbitrarily set weights, and by 10.7% compared to the plans generated by human planners.	[110]
Intra-fractional OARs dose-volume histogram prediction	GYN	30	ANN	MPE = 6%, 5%, 8%, 7%, 10% for predicting intra-fractional dose variations of bladder, rectum, sigmoid, CTV_{IR} , and CTV_{HR} , respectively.	[55]
Optimizing Treatment Parameters	Prostate	35	MANN and GA	The optimal values for Therapy Dose (TD) = 47.3 Gy, TD coverage index ($CI_{100\%}$) = 1.14, and PSA nadir = 0.047 ng cm^{-3} for low-risk group; TD = 50.4 Gy and $CI_{100\%}$ = 1.6, and PSA nadir = 0.25 ng cm^{-3} for high-risk group.	[97]

Note: Abbreviations: MRAE (mean relative absolute error), VGG-16 (16-layers CNN developed by the visual geometry group), SVM (support vector machine), RSDM (rectum surface dose maps), LM (Levenberg–Marquardt), ANN (artificial neural network), MANN (multilayer artificial neural network), GA (genetic algorithm), MO-RV-GOMEA (multi-objective real-valued gene-pool optimal mixing evolutionary algorithm), BRIGHT (brachytherapy via artificial Intelligent GOMEA-Heuristic based treatment planning), Rad-TRaP (radiomics based targeted radiotherapy planning).

5 Applicator Reconstruction

5.1 GYN

Accurate digitization of applicators and catheters is crucial in HDR GYN treatment planning as it largely affect the final dose distribution. Table 7 provides a summary of the AI implementation in different types of applicator reconstruction, such as the T&O, tandem & ring (T&R), fletcher applicators, catheters, and needles. To automatically segment the T&O applicators on CT images, Jung et al. [57] trained a U-net model with additional spectral clustering and polynomial curve-fitting methods to identify the locations and the central paths of applicators. Although trained solely on CT images T&O applicators, the model accurately digitized not only T&O applicators but also Y-tandem and cylinder applicators on CT, as well as T&O applicators on cone-beam CT. Both tip position errors and HD were less than 1 mm under various testing setup, indicating the model’s robustness and transferability when applied to different applicator structures and lower image quality.

MRI provides better visibility of soft tissue but has difficulty imaging applicators due to the inconsistent appearance of contrast fiducials on the applicator lumen. However, HDR cervical brachytherapy applicators can be reconstructed using MRI alone with library applicator models from the manufacturers, which is potentially more reproducible than digitization on CT images. Hrinovich et al. [47] utilized a circular Hough transform (CHT) model [24] to identify tandem and ring applicators on T2-weighted MR images. It is followed by a 3D rotation matrix and a 3D translation vector with a stochastic evolutionary optimizer [114] to obtain the positions of T&R applicators with a rigid registration method. The proposed method achieved a mean reconstruction accuracy of 0.60 ± 0.24 mm for the ring and 0.58 ± 0.24 mm for the tandem, with mean variability smaller than the inter-observer variability. Plastic catheters have a low hydrogen composition, which makes them difficult to identify on the MRI. Zaffino et al. [142] developed a 3D U-Net model to automatically segment multiple closely spaced brachytherapy catheters in MRI. The model produced a good accuracy with an average distance error of 2.0 ± 3.4 mm, DSC of 0.60 ± 0.17 , and a HD of 15.9 ± 20.5 mm. The false positive and false negative catheters were 6.7% and 1.5%, respectively. Similar results were provided by Shaaer et al. [108], as outlined in Table 7. The accuracy of the segmentation struggled with tubular structure reconstruction, especially on MR images where other tubular tissue structures exist.

TABLE VII. AI in GYN applicator reconstruction

Type of Applicator	Image Modality	Number of Patients	Model	Results	Citation
T&O applicator	CT	13	U-Net	For applicator segmentation: DSC = 0.937 ± 0.064 in 2D and 0.931 in 3D. HD = 1.01 mm, 1.21 mm, and 1.18 mm. For tip position errors: tandem = 0.5 mm, right ovoid 0.74 mm, and left ovoid = 0.67 mm.	[57]
T&O applicator	CT	91	DSD-UNET	For the intrauterine and ovoid tubes: DSC = 0.921, HD = 2.3 mm. Between channel paths: HD = 0.88 ± 0.12 mm, 0.95 ± 0.16 mm, and 0.96 ± 0.15 mm for the intrauterine, left ovoid, and right ovoid tubes, respectively.	[146]
T&O applicator	CT	10	HDBSCAN	Mean contour error = 0.3 mm, HD _i =1 mm. For HR-CTV D_{90} , HR-CTV D_{95} , bladder D_{2cc} , rectum D_{2cc} , large bowel D_{2cc} , and small bowel D_{2cc} , the median and mean difference in DVH parameters are all $\leq 1\%$.	[21]
Fletcher applicator	CT	70	U-Net	For applicator segmentation: DSC = 0.89 ± 0.09 , HD = 1.66 ± 0.42 mm, shaft error ≤ 0.5 mm, tip error = 0.8 mm. Dosimetric differences = 0.29% for the D_{90} of HRCTV, and less than 2.64% for OAR D_{2cc} .	[48]
T&R applicator	MRI	10	CHT	For dwell positions, the mean errors = 0.60 ± 0.24 mm and 0.58 ± 0.24 mm, variability = 0.72 ± 0.32 mm and 0.70 ± 0.29 mm, and inter-observer variability = 0.83 ± 0.31 mm and 0.78 ± 0.29 mm, for the ring and tandem, respectively.	[47]
Catheters	MRI	50	3D U-Net	DSC = 0.60 ± 0.17 , HD = 15.9 ± 20.5 mm, MDE = 2.0 ± 3.4 mm, false positive = 6.7%, and false negative = 1.5%.	[142]
Catheters	MRI	20	2D U-Net	DSC = 0.59 ± 0.10 and HD = 4.20 ± 2.40 mm. Average variation = 0.97 ± 0.66 mm with 98.32% ≤ 2 mm and 1.68% ≥ 3 mm	[108]
Interstitial needles	CT	15	2.5D U-Net	DSC = 0.93 for needle segmentation, HD = 0.71 mm for needle trajectories, and HD = 0.63 mm for needle tip positions.	[58]
Interstitial needles	CT	17	3D U-Net with attention gates	DSC = 0.937 ± 0.014 , JI = 0.882 ± 0.025 , HD = 3.0 ± 1.9 mm, tip error = 1.1 ± 0.7 mm, and shaft error = 1.8 ± 1.6 mm	[128]
Needle structures	Ultrasound	5 prostate patients, 6 GYN patients	CNN with modified U-Net	For prostate: needle tip error = 1.5 [0.9, 8.3] mm, angular error = 0.4 [0.3, 0.7] °, HD = 6.8 [1.3, 17.6] mm, DSC = 0.789 [0.738, 0.847], recall = 73.2 [62.4, 81.9] %, and precision = 87.9 [84.8, 95.8] %. For GYN: needle tip error = 0.3 [0.2, 0.4] mm, angular error = 0.4 [0.2, 0.7] °, HD = 0.5 [0.4, 0.9] mm, DSC = 88.7 [84.6, 93.5] %, recall = 85.2 [80.9, 91.1] %, and precision = 93.2 [89.6, 97.0] %.	[32]
T&R applicator and interstitial needles	CT	48	nnU-Net and 3D U-Net	DSC = 0.646 for T&R applicators and 0.738 ± 0.034 for interstitial needles.	[16]

Note: Abbreviations: HDBSCAN (density-based linkage clustering algorithm), DSD-UNET (dilated convolution and deep supervision U-Net). Duplicate paper from Zhang et al. [146] as in Table 2.

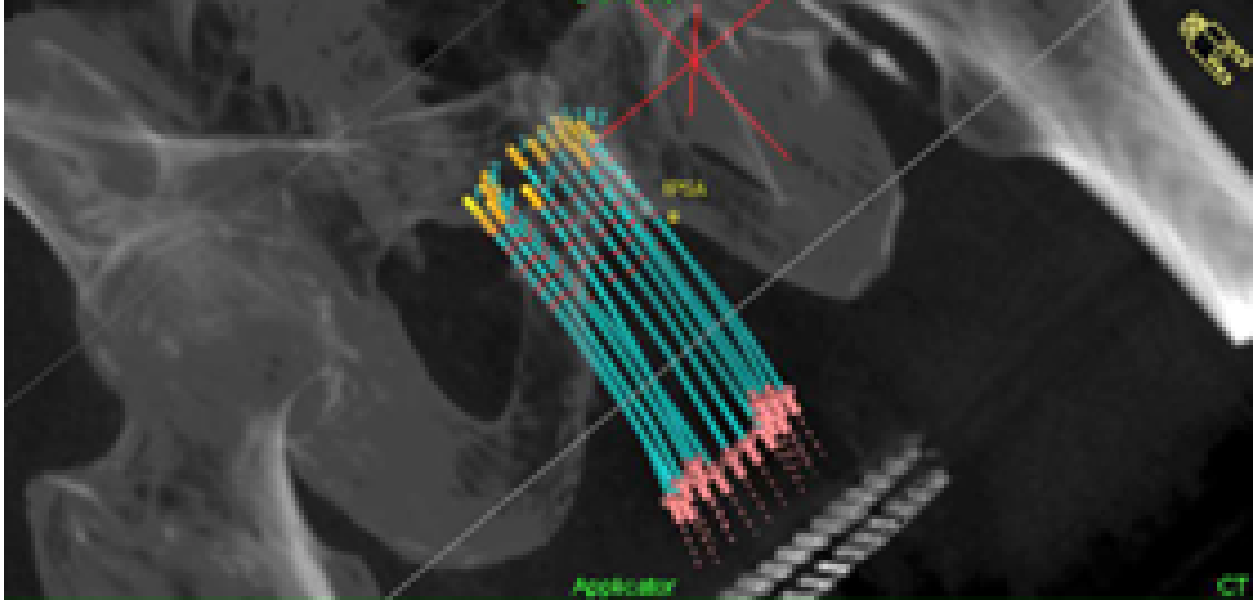


Figure 8. Needle reconstruction on CT image for HDR prostate brachytherapy.

5.2 Prostate

For prostate brachytherapy, both HDR and LDR, are unique procedures with comparable workflow and distinct advantages [143]. As detailed in Table 8, approximately the same number of studies used deep learning to assist HDR applicator reconstruction (identifying needles and catheters) and LDR (reconstructing needles and seeds under different imaging modalities). HDR brachytherapy for prostate cancer involves the insertion of interstitial needles through the perineum, followed by imaging using techniques such as TRUS, MRI, or CT. TRUS is the most common imaging modality used to guide the insertion of needles for HDR prostate brachytherapy. Andersén et al. [8] used a 3D CNN U-Net model to identify needles in TRUS images. The model was trained on a large dataset consisting of 1102 brachytherapy treatments, with a total of 24422 individual needles. The model achieved a root-mean-square distance (RMSD) of 0.55mm compared to the clinical ground truth and 0.75 mm compared to another physicist’s digitization, which is lower than the inter-observer variability of 0.80 mm. To further enhance the needle digitization workflow, Zhang et al. conducted three studies using different deep-learning approaches to detect multiple needles on 3D TRUS images simultaneously. The three approaches were using an order-graph regularized dictionary learning (ORDL)-based method [148], a deeply supervised attention U-Net with a total variation (TV) regularization method [149], and a large margin mask R-CNN model (LMMask R-CNN) with a needle-based density-based spatial clustering method [150]. The shaft and tip errors and accuracies were similar in all three methods but the LMMask R-CNN-based model had the most superior result, detecting 98% of needles with shaft and tip errors of 0.091 ± 0.043 mm and 0.33 ± 0.363 mm, respectively.

CT images can also be used to reconstruct the needles, as illustrated in Figure 8. Weishaupt et al. [129] developed a deep-learning method to automatically digitize the HDR prostate needles on CT images. Using 2D U-Net architecture, the model segmented the catheters and reconstructed their geometries in 3D using a density-based linkage clustering algorithm. The model accurately digitized all needles in under one minute with a mean tip distance difference of -0.1 ± 0.6 mm and a mean shaft distance of 0.13 ± 0.09 mm. This method is highly efficient when compared to manual approach, which typically takes an average of two minutes per needle.

MRI-guided HDR prostate brachytherapy has the potential to optimize the dose distribution due to MRI’s superior visualization of the DIL compared to TRUS or CT. [93] However, digitizing catheters in MRI is challenging because of their dark and diffuse appearance. To address this issue, Dai et al. [19] utilized an attention-gated U-Net to automatically digitize catheters and a TV regularization to remove excessive noise. The catheter tip error was found to be 0.37 ± 1.68 mm, with 87% of the tips within localization error of no greater than 2.0 mm. Regarding catheter shaft localization, the error was 0.93 ± 0.50 mm, with 97% of catheters detected with an error of less than 2.0 mm. The precision, recall, and F1 score of shaft localization were 0.96, 0.86, and 0.91, respectively. These results indicate that AI

can simplify catheter digitization on MRI, potentially facilitate the use of MRI-guided brachytherapy in clinical practice and leading to improved patient outcomes.

During the LDR prostate brachytherapy procedures, the placement of the radioactive seeds is guided by TRUS and often updated based on real-time changes in the prostate. It is crucial to compare the locations and orientations of implanted seeds to the planned seeds to adjust plans accordingly before the next seed implantation. Golshan et al. [35] implemented a CNN model with a coarse sliding window approach to identify the needle tracks, then detect stranded seeds within each identified track. It achieved a precision of $78 \pm 8\%$, recall of $64 \pm 10\%$, and an F1 score of $70 \pm 8\%$. The relatively low recall suggests that many seeds were not identified on TRUS images, primarily due to poor ultrasound image quality and a small training cohort. Due to similar challenges, Holupka et al. [46] was also not able to provide high identification precision for loose seeds on TRUS.

CT is commonly used to assess LDR treatment quality post-implant. Nguyen et al. [81] used several machine learning-based models to segment single seeds and groups of closely spaced (union) seeds on CT images. They first used a k-means method to categorize the seeds into single or union seeds groups, then a modified k-means for seeds (k-means-FS) and a Gaussian mixture model (GMM) with expectation-maximization (EM) method to separate the union seed groups. The training and testing dataset comprised 14 patients with a total of 1063 implanted seeds, along with two phantoms (1 seed and 73 seeds). The seed angular orientation errors and MDE were greater in patients compared to the phantoms due to the complex anatomical structures, and the false detection rate ranged from 1.8% to 4.8% for different setups.

The implanted radioactive seeds can also be identified on MRI only, as it offers superior soft tissue contrast than CT. However, it can be challenging since they do not produce MR signals. An endorectal coil (ERC) can enhance seed visibility on MRI scans but may entail additional costs and discomfort for patients. To reduce the manual labor of identifying radioactive seeds on MRI after LDR brachytherapy, Sanders et al. [104] developed a sliding-window CNN algorithm (SeedNet), which automatically identifies implanted radioactive seeds on prostate MRI scans. SeedNet demonstrated superior accuracy and reduced identification time compared to results from dosimetrists for patients both with and without an ERC. With ERC, seed detection achieved the highest recall (97.6%), precision (97.2%), and F1 score (97.4%). Additionally, detection exhibited a low false discovery rate (2.8%), low false-negative rate (2.4%), and low root mean square error (RMSE) of $0.19 \text{ mm} \pm 0.04 \text{ mm}$, all within an inference time of 56.6 ± 18.2 seconds.

6 Quality Assurance (QA)

Brachytherapy QA includes multiple aspects, such as safety, equipment, and plan QA. While the safety and equipment QAs are typically performed manually before the treatment delivery, the plan QA can be performed with the assistance of AI to identify suboptimal plans and improve plan qualities. Three studies used AI models to assist the plan QA, as summarized in Table 9. Reijtenbagh et al. [99] trained an RF model using Overlap Volume Histograms (OVHs) to predict the DVH for each OAR in HDR GYN brachytherapy. It predicted doses for the target, bladder, rectum, sigmoid, and small bowels, allowing perform patient anatomy-based QA. This QA model detected sub-optimal plans by identifying when D_{2cc} values fell outside the 95% confidence interval, showing strong correlation with MSE ranged between 0.13 and 0.40 Gy. Testing on a different institution's data, the model identified several clinically compliant plans, proving the model's effectiveness in multi-center settings. The OVH-based QA model also has advantage in its short training time of less than a minute and short prediction times within seconds. Reijtenbagh et al. [100] found an average reduction of 0.62 Gy for all OARs utilizing their QA model, further proving its effectiveness. Another group from EMC [90] utilized a fully automated planning model (Erasmus-iCycle) and successfully reduced a mean D_{2cc} of 0.87 Gy in bladder and 1.4 Gy in rectum, yet the study was constrained to single-institute setting. Further, Fan et al. [28] developed a DNN model for HDR brachytherapy plan QA, focusing on checking dwell times and positions. The model, based on Inception network by Szegedy et al. [116], used a small number of parameters to reduce the computation burden and the risks of overfitting in traditional CNN methods. Given the non-linear nature of the regression problem, Fan et al. employed a heatmap to represent the probability distribution of the dwell position, reducing the complexity of the task. Predictions of dwell times were within a 2% deviation from the ground truth, and dwell positions were within one pixel of the planned

TABLE VIII. AI in prostate applicator reconstruction

Type of Ap- plicator	Image Modality	Number of Patients	Model	Result Summary	Citation
Needles	TRUS	1102	3D CNN U-Net	RMSD = 0.55 [0.35 0.86] mm	[8]
Needles	TRUS	21	ORDL	Shaft error = 0.19 ± 0.13 mm, tip error = 1.01 ± 1.74 mm, accuracy = 0.95	[148]
Needles	TRUS	23	Deep supervised attention U-Net	Shaft error = 0.29 ± 0.23 mm, tip error = 0.44 ± 0.93 mm, accuracy = 0.96	[149]
Needles	TRUS	23	LMMask R-CNN	Shaft error = 0.091 ± 0.043 mm, tip error = 0.330 ± 0.363 mm, accuracy = 0.98	[150]
Needles	TRUS	823	Modified deep U-Net and VGG-16	Needle trajectories: resolutions = 0.668 mm and 0.319 mm in x and y direction. Needle tips: resolution = 0.721 mm, 0.369 mm, and 1.877 mm in x, y, and z directions.	[123]
Catheters	TRUS	242	U-Net and 3D reconstruction	80% of catheter reconstructions were accurate within 2 mm along 90% of the catheter lengths. Reconstruction accuracy = 91% excluding 27% outliers.	[73]
Catheters	TRUS	49	3D U-Net	AUC = 0.85, recall = 0.97, and true positive rate = 0.95.	[49]
Needles	CT	57	U-Net	Mean tip distance difference = -0.1 ± 0.6 mm with range from -1.8 mm to 1.4 mm. Mean shaft distance = 0.13 ± 0.09 mm with maximum distance = 0.96 mm.	[129]
Catheters	MRI	20	Deep supervised attention U-Net	Precision = 0.96, recall = 0.86, F1 = 0.91. Catheter tips localization: error = 0.37 ± 1.68 mm, 87% with errors less than ± 2.0 mm, and more than 71% within 1.0 mm. Catheter shaft localization: error = 0.93 ± 0.50 mm, 97% with errors less than ± 2.0 mm, and 63% within 1.0 mm.	[19]
Catheters	MRI	35	3D U-Net	F1 score = 0.73, precision = 0.65, recall = 0.85, percentage of needles detected = 97.5%	[5]
Stranded Seeds	TRUS	13	CNN	Precision = $78 \pm 8\%$, recall = $64 \pm 10\%$, F1 score = $70 \pm 8\%$	[35]
Needles	TRUS	9	Bayesian classifier	23 fully visible needles: mean tip error = 1.4 mm, mean axis error = 1.5° . 19 partially visible needles: mean tip error = 4.2 mm, mean axis error = 6° .	[136]
Stranded and Loose Seeds	TRUS	1 phantom	Bayesian classifier and SVM	Mean error = $1.09 \text{ mm} \pm 0.61 \text{ mm}$ on phantom image and $1.44 \pm 0.45 \text{ mm}$ on clinical images. Angle orientation error = $4.33 \pm 8.5^\circ$.	[137]
Loose Seeds	TRUS	10	DetectNet	Location error = 2.29 mm, precision = 81.07% and recall = 82.29%.	[46]
Loose Seeds	CT	14 patients and 1 phantom	k-means, k-means-FS, and GMM with EM method	For the phantom, the angular orientation error = $0.96 \pm 0.4^\circ$, and MDE = 0.08 ± 0.04 mm. For the patient, the maximum angular orientation error = $3.18 \pm 0.9^\circ$, and MDE = 0.50 ± 0.16 mm. The least false detection rate = 1.8%	[81]
Stranded Seeds with Positive Contrast MR-signal Seed Markers	MRI	68	SeedNet	With ERC: seed localization recall = $97.6 \pm 2.2\%$, precision = $97.2 \pm 1.9\%$, F1 score = $97.4 \pm 1.5\%$, and RMSE = 0.19 ± 0.04 mm. Without ERC: seed localization recall = $96.5 \pm 2.3\%$, precision = $90.5 \pm 4.6\%$, F1 score = $93.3 \pm 3.0\%$, and RMSE = $0.24 \text{ mm} \pm 0.03 \text{ mm}$.	[104]
Stranded Seeds	MRI	1 phantom	QSM, k-means, and k-medoids clustering	The average length and width of detected seeds = $4.6 \pm 0.3 \text{ mm}$ and $0.9 \pm 0.2 \text{ mm}$, compared with the actual dimensions of 4.5 mm and 0.8 mm. Maximum seed centroids difference = 7 mm. Dose distribution differences range from -8 to 8 Gy/U.	[85]

Note: Abbreviations: VGG-16 (16-layers CNN developed by the visual geometry group), SVM (support vector machine), QSM (quantitative susceptibility mapping).

TABLE IX. AI in QA

QA Tasks	Cancer Site	Number of Patients	Model	Result Summary	Citation
Predict dose-volume histograms	GYN	145	RF	MSE between planned and predicted OARs D_{2cc} ranged between 0.13 and 0.40 Gy	[139]
Treatment Plan QA	GYN	34	Erasmus-iCycle	62 out of 63 plans were comparable or better than clinically generated plans, desired dose obtained in 14 out of 16 plans.	[141]
Predict dwell positions and times	GYN	130	DNN	Dwell times prediction error within 2% from the ground truth, dwell positions within one pixel of the planned positions.	[142]

positions. Despite the long training time of the model, it offered fast and accurate plan QA, predicting dwell times and positions within seconds.

7 Outcome Prediction

AI demonstrates proficiency in predicting clinical outcomes, aiding oncologists and physicists can make informed decisions regarding patient treatment. As summarized in Table 10, three different outcome prediction tasks are carried out by machine learning models for both prostate and GYN brachytherapy. Two studies utilized ML methods to make the predictions for locally advanced cervical cancer (LACC) patients. Abdalvand et al. [1] studied the effectiveness of four different ML algorithms, LASSO (Least Absolute Shrinkage and Selection Operator) regression, Ridge regression, support vector machine (SVM), and RF in terms of LACC outcome prediction. The ten most important features when considering LACC outcomes were selected from LASSO algorithm to reduce complexity and mitigate over-fitting. The study specifically incorporated patient-specific applicator insertion geometries from 3D MR or CT imaging, as well as the physical, dosimetric, radiobiological, and clinical factors when training the models. The RF algorithm had the highest discriminating ability with an area AUC of 0.82, but an accuracy of only 0.77, limited by the small patient sample (111 selected) and the traditional ML model's ability to address heterogeneities of the clinical data. Tian et al. [118] devised a nonlinear kernel based SVM classifier to predict fistula formation from the high radiation doses in patients undergoing interstitial brachytherapy for LACC. Using sequential backward selection and sequential floating backward selection methods, Tian et al. identified 7 most crucial features for model training. Consequently, their model achieved an AUC of 0.904, with sensitivity and specificity rates of 97.1% and 88.5%, respectively.

The recurrence rate of prostate cancer after the initial treatment can be predicted with ML models, offering potential guidance in identifying patients who would benefit the most from salvage HDR brachytherapy. Valdes et al. [120] used MediBoost (a decision-tree based model built by the same group [119]) and a classification and regression tree (CART) model to predict the 5 years recurrence rate. Only the most important features were selected such as the percentage of positive cores after biopsy and disease-free interval after the first definitive treatment to reduce complexity and risk of over-fitting of the data. The study found a 5-year recurrence probability of 0.75 associated with positive cores $\zeta = 0.35$ and a disease-free interval $\eta = 4.12$ years. Although the study was limited by the small dataset of 52 patients, there is 70% probability that the results were not due to random variation.

8 Real-time Monitoring

While various devices and systems can achieve real-time monitoring of HDR brachytherapy, AI offers an alternative solution that enhances quality and efficiency, as detailed in Table 11.

Malignant tumors frequently exhibit distinct temperature distributions compared to normal tissue. Therefore, thermal imaging can aid in identifying tissue-specific changes in the cervix during brachytherapy that are necessary for plan adjustments. Hoffer et al. [45] used the k-means method to predict the

TABLE X. AI in brachytherapy outcome prediction

Application	Cancer Site	Number of Patients	Model	Result Summary	Citation
Cervical cancer outcome prediction	GYN	111	LASSO, Ridge, SVM, and RF	Best AUC = 0.82, sensitivity = 0.79, specificity = 0.76, and accuracy = 0.77	[1]
Predict fistula development from high radiation dose	GYN	35	Nonlinear kernel-based SVM classifier	AUC = 0.904, sensitivity = 97.1%, and specificity = 88.5%	[118]
Select patients to receive salvage HDR brachytherapy after first recurrence after radiation therapy	Prostate	52	CART and MediBoost	Positive cores $\zeta = 0.35$ and a disease-free interval $\eta = 4.12$ years has a second recurrence rate of 0.75, the conclusion has a 70% probability of not due to random variations	[120]

status of the cervix before and after brachytherapy, using skewness and entropy levels from the thermal image of the cervix. Additionally, K Nearest Neighbors (KNN) and SVM validated a 100% detection rate for structural and textual changes in cervical tumors before and after brachytherapy.

During HDR brachytherapy treatments, monitoring the source position and dwell times of the radioactive source can be achieved through a gamma camera, which often suffers from blurring effect and noise. Nakanishi et al. [80] proposed a DL based approach to estimate the actual image without blurring effect and noise for better real-time monitoring of the Ir-192 source. The method consisted of two P2P models, similar to the method provided by Isola et al. [54] The highest structural similarity index measure (SSIM) value was 0.980.006 and the lowest MAE was $2.210^{-3}110^{-3}$. Additionally, the full width at half maximum (FWHM) of the estimated image in both horizontal and vertical directions differed by less than 0.5 mm from the actual source size.

Finally, AI can be used in the calibration of plastic scintillation detectors in a multi-point configuration (mPSD), which provides in-vivo dosimetry measurement and real-time source tracking. Rosales et al. [72] trained and compared three algorithms, linear regression, RF, and ANN to calibrate mPSD for real-time feedback in HDR brachytherapy. Among the tree algorithms, the RF had the most accurate calibration result with dose deviation generally remained below 20% and below 2% when same range of distances was used for calibration. This ML-based method requires only one calibration for the detector but can still be time-consuming if calibration at multiple locations is needed. While improvements are still needed, this algorithm can lead to more precise measurements of mPSD and help medical physicist and oncologists with adjusting treatment plans.

9 Discussion

In this review, we summarized AI's applications in different parts of brachytherapy workflows, highlighting its comparable performances to manual efforts in the segmentation, classification, and prediction tasks with non-significant errors.

The imaging section has the most studies, this is because AI's role in brachytherapy largely relies on imaging tasks. With the advent of deep learning, image registration has not only become more efficient but also more feasible, especially in terms of achieving precise multi-modal registration. Fast and accurate multi-model image registration is particularly valuable in brachytherapy, where integrating MRI information with TRUS can provide better guidance during the procedure. Besides MRI-TRUS fusion, AI can also enhance resolution and reduce artifacts, providing an alternative solution to overcome imaging challenges in brachytherapy.

TABLE XI. AI in brachytherapy real-time monitoring

Monitoring Application	Cancer Site	Number of Patients	Model	Results	Citation
Monitor thermal image to predict structural and textual changes in cervical tumors before and after brachytherapy	GYN	6	k-means, KNN, and SVM	100% detection rate for physiological changes in cervical tumors before and after brachytherapy	[45]
Reduce blurring and statistical noise in real-time monitoring of Ir-192 sources with gamma camera	GYN	11	Pix2pix models	The highest SSIM = 0.98 ± 0.006 and MAE = $2.2 \times 10^{-3} \pm 1.0 \times 10^{-3}$. FWHM error 0.5 mm in both horizontal and vertical directions.	[80]
Calibration of mPSD	GYN and Prostate	1936 dwell positions	Linear regression, RF, and ANN	Dose predictions accuracy within 7% of the TG-43 U1 formalism with all models and less than 2% deviations using RF model	[72]

Manual contouring is time-consuming and requires extensive training, while AI models can learn segmentation techniques in hours or less. Most studies reported AI segmentation is dramatically faster than human experts on all image modalities. Kraus et al. [64] demonstrated that using AI in clinical workflows reduces and standardizes the time from contouring to approval, with AI workflows taking 71–111 minutes, compared to the large deviation of 29–304 minutes with manual workflows. AI’s efficiency stems not only from its rapid processing capabilities, but also from the absence of clinical interruptions that human physicians frequently encounter. The reviewed studies showed that AI-generated contours often closely resemble those produced manually in quantitative evaluations. Several other studies have also shown AI’s superior segmentation from different perspectives. For instance, Sanders et al. [106] evaluated the differences in dosimetric parameter between the prostate and OAR contours generated solely by a deep-learning algorithm (MIM-Symphony) and those further refined by physicians, finding no significant differences in the dosimetric parameters even after human refinement. King et al. [62] conducted a survey on prostate contours on TRUS images generated by AI versus by professionals. The AI algorithm, using nnU-Net, generated contours with median DSC of 0.92 and won a median of 57.5% of clinical observer preference, showing strong performance both objectively and subjectively. In addition, AI can standardize contours and reduce inter-observer variability errors. As shown in Andersén’s [8] study, their deep learning model produced results with errors smaller than inter-observer variability.

Studies on AI applications in treatment planning suggest that AI can generate plans that are comparable to, or even superior to, those created by human planners. This capability stems from AI’s ability to learn from hundreds of high-quality treatment plans during its training phase. While manual planning can indeed produce excellent results, it is heavily reliant on the planner’s experience and is often resource-intensive and time-consuming. In contrast, AI can generate superior plans much more efficiently. The plan check function from automatic dose prediction models can also detect sub-optimal plans that require proper adjustments.

AI application in applicator reconstruction, particularly multi-needle digitization, offer the potential to facilitate real-time treatment planning and dosimetric adjustments, mitigating discrepancies between the planning stage and the operating room, although there are still challenges in ground truth contour accuracy and needle trajectory prediction. AI models have the potential to simplify more advanced procedures, such as MRI-guided brachytherapy. Overall, AI can improve brachytherapy workflow efficiency, producing similar results to conventional methods in significantly less time with more consis-

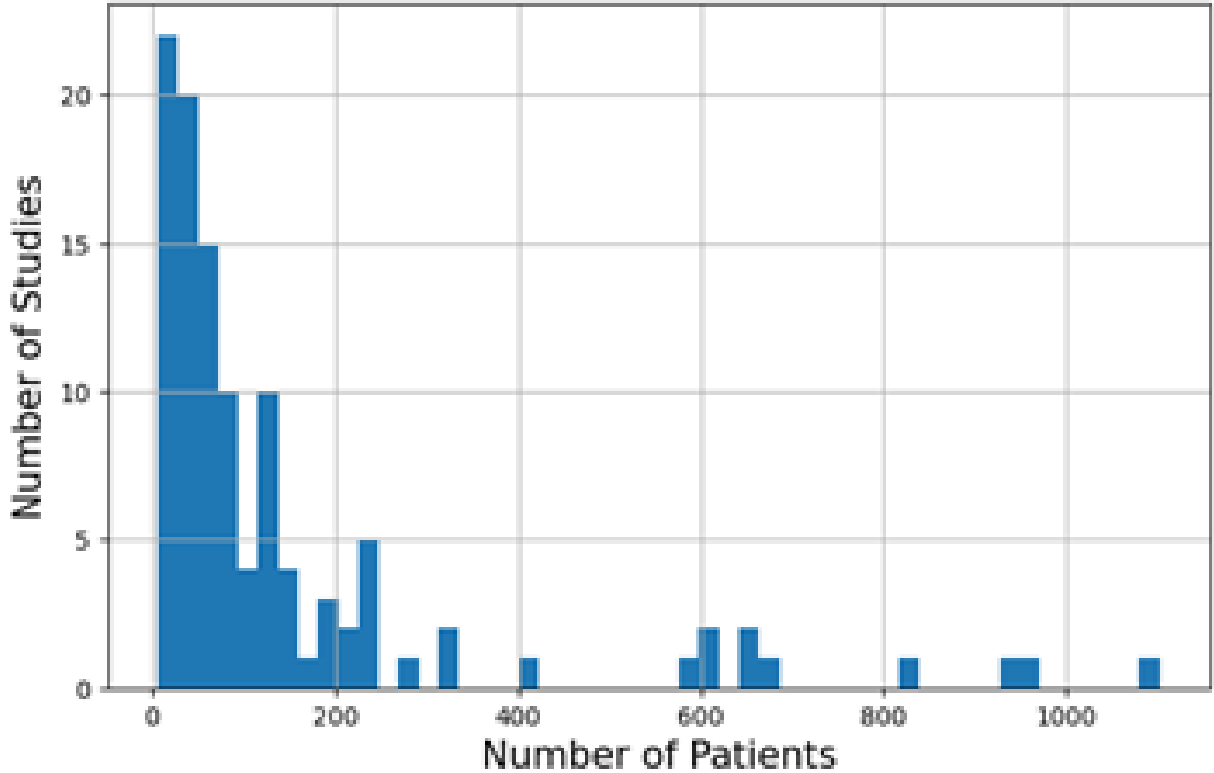


Figure 9. Distribution of Number of Patients in investigated studies.

tency.

The outcome prediction, QA, and real-time monitoring sections have the least AI application for several reasons. While AI can assist with brachytherapy preparation, the treatment quality heavily depends on the skills of the physicians or surgeons in the operation room, and physicists responsible for monitoring source delivery and performing QA. The human-centered nature of QA and real-time monitoring limits AI integration in these areas. Outcome prediction, however, is particularly challenging due to the need for long-term data, which is often limited. This lack of comprehensive patient data makes it difficult to apply AI effectively in predicting outcomes, as the reviewed studies only included 35, 52, and 111 patients.

Two common limitations for the current application of AI in brachytherapy are the small patient cohorts and single institution setups. Analyzing patient numbers involved in each study, we found the mean and the median numbers to be 149 and 66, respectively. A histogram in Figure 9 illustrates the distribution, showing skewness due to a few studies with exceptionally large patient cohorts, while most studies have less than 200 patients. Despite the advantages of brachytherapy, such as shorter overall treatment time and positive outcomes compared to surgery or EBRT [38], there has been a general decline in its use [92]. This is due to procedural difficulty and a reduction in residency brachytherapy training, which has decreased the number of physicians competent in performing this procedure [130].

Many studies addressed this challenge by employing cross-validation methods, in which the total available data is partitioned into several groups, with one group for validation and the rest for training. The training of the model ends when each group is used as the validation set once. The cross-validation methods allow the maximum utilization of available data for training and validation by assessing the model's performance across different subsets and enhancing its reliability and generalizability. Data augmentation, which involves applying elastic deformations or transformation such as rotating and resizing, allows different U-Net-based models to gain more training dataset and learn invariance to deformations. Besides, transfer-learning can also be used to leverage the challenge of limited data size, several studies [4, 82, 105, 140, 151] showed that fine-tuning with limited clinical data could lead to more precise task outcomes although requiring longer training times.

Although various methods exist to mitigate the adverse effects of limited image data, addressing the

challenge posed by the lack of patient anatomy and setup variations remains difficult. For example, Holupka et al. [46] used 950 training US images from 10 patients, resulting in large seed location errors as large as 2.29 mm when evaluated on new patient sets due to lack of patient variation. AI models may struggle anatomies deviating significantly from training datasets, making reliance on AI-generated results risky, particularly in HDR settings. Diverse data, in terms of various tumor sites, heterogeneities, shielded applicators, and different radiation sources, is crucial for obtaining a model suitable for general-purpose brachytherapy dosimetry [77].

Another significant issue in current AI studies is the reliance on training data from single institutions. Brachytherapy procedures are heavily dependent on imaging protocols, and AI models trained on data from one institution may not perform well elsewhere. Although there were a few studies [69?] showed no statistically significant difference in cross-institution testing, majority of studies lack this validation. Even using the same imaging protocol, applicator types for brachytherapy could vary, further complicating the implementation of pretrained models [18, 100]. For example, in the applicator reconstruction of cervical cancer brachytherapy section, most of the applicator reconstruction studies used T&O applicators, but the studies on other types of applicators, such as the T&R and Fletcher applicators, could be further investigated. Although the geometries of applicators may be somewhat similar, it is challenging to apply a model trained on one type of applicator to another type. Dose prediction tasks can be complex due to applicator variability, typically involving one type of applicator setup per study. In addition, the acceptability of AI predicted plans is heavily reliant on the quality of clinical ground truth, influenced by variability in treatment planning system and protocol adopted in each institution. Therefore, future generalized AI models development should include large and diverse patient datasets from multiple institutions to address these limitations [99].

One potential solution for these common issues is to implement foundation models, especially in the field of imaging. Segment Anything Model (SAM) [63], introduced by the Meta AI Research team, is a foundation model for segmenting any object in the input image by detecting valid masks within images and operating through a supervised routine rather than relying solely on unsupervised learning. SAM was pre-trained on a comprehensive dataset with over 1 billion masks sourced from 11 million images. This extensive training employs a task that promotes robust generalization, enabling zero-shot adaptability to unfamiliar objects and images without necessitating supplementary training. Following the introduction of SAM, Ma et al. introduced MedSAM [76], a refined foundation model that specifically integrates medical knowledge to segment medical images. It is designed for universal segmentation tasks and trained on a vast and diverse dataset of over a million medical image-mask pairs that cover 15 modalities and 30 cancer types. MedSAM addresses the issue of the task-specific nature of previous models, which are only capable of segmenting certain image modalities or specific tissues. The diversity in data sources effectively eliminates the need for additional training, addressing the limitation of large biomedical image datasets. MedSAM's capability to manage various anatomical structures and imaging modalities makes it a potential tool for brachytherapy imaging applications. Large foundation models such as MedSAM can be integrated with fine-tuning methods for more accurate organ segmentation [39], which is applicable to brachytherapy procedures. Future studies aiming to automate the segmentation of organs, tumors, or applicators can achieve this by fine-tuning these models, even with limited, single-institution datasets, potentially leading to more reliable results that are acceptable clinically. Since many aspects of brachytherapy, such as image registration, treatment planning, and applicator placement, depend heavily on accurate image segmentation, the implementation of large foundation models could offer a possible solution to the current challenges in applying AI to brachytherapy.

The final issue with current implementation of AI is the lack of universal standards in evaluating the performance of AI models. While image segmentation has some commonly accepted evaluation methods, other aspects lack clear reporting guidelines, making it difficult to compare the results of different AI models. Without consistent metrics for comparison, identifying areas for improvement and proposing clear solutions for future studies becomes challenging. The establishment of universal evaluation guidelines for each procedure category is necessary to ensure the future improvement of AI application, thereby enhancing brachytherapy treatments.

10 Conclusion

This review covers the current development of AI in brachytherapy, focusing on prostate and GYN cancer treatments. Unlike EBRT, which benefits from extensive patient data and straightforward AI implementation, brachytherapy requires additional manual procedural accuracy, introducing unique difficulties for AI integration. Current challenges include the lack of patient data from diverse institutions, and a possible solution is to adopt new foundational models to enhance image segmentation, which paves the way for improvements in other procedures as well. Establishing universal standards in validating the application of AI in brachytherapy is also essential to improve AI's performance. Despite these challenges, AI has the potential to enhance image segmentation accuracy, provide high-quality plans, simplify real-time planning, which significantly enhance the brachytherapy workflow and encourage the use of brachytherapy. By addressing these challenges and investing in further development, AI can improve the quality of brachytherapy treatment and patient outcomes in the foreseeable future.

ACKNOWLEDGEMENT

This research is supported in part by the National Institutes of Health under Award Number R01CA215718, R01DE033512, R01CA272991 and P30CA008748.

Disclosures

The authors declare no conflicts of interest.

References

- [1] N. Abdalvand, M. Sadeghi, S. R. Mahdavi, H. Abdollahi, Y. Qasempour, F. Mohammadian, M. J. T. Birgani, and K. Hosseini. Brachytherapy outcome modeling in cervical cancer patients: A predictive machine learning study on patient-specific clinical, physical and dosimetric parameters. *Brachytherapy*, 21(6):769–782, 2022. ISSN 1873-1449 (Electronic) 1538-4721 (Linking). doi: 10.1016/j.brachy.2022.06.007. URL <https://www.ncbi.nlm.nih.gov/pubmed/35933272>.
- [2] A. Akhavanallaf, R. Mohammadi, I. Shiri, Y. Salimi, H. Arabi, and H. Zaidi. Personalized brachytherapy dose reconstruction using deep learning. *Comput Biol Med*, 136:104755, 2021. ISSN 1879-0534 (Electronic) 0010-4825 (Linking). doi: 10.1016/j.compbimed.2021.104755. URL <https://www.ncbi.nlm.nih.gov/pubmed/34388458>.
- [3] T. A. Aleef, I. T. Spadinger, M. D. Peacock, S. E. Salcudean, and S. S. Mahdavi. Centre-specific autonomous treatment plans for prostate brachytherapy using cgans. *Int J Comput Assist Radiol Surg*, 16(7):1161–1170, 2021. ISSN 1861-6429 (Electronic) 1861-6410 (Linking). doi: 10.1007/s11548-021-02405-1. URL <https://www.ncbi.nlm.nih.gov/pubmed/34050909>.
- [4] Tajwar Abrar Aleef, Ingrid T Spadinger, Michael D Peacock, Septimiu E Salcudean, and S Sara Mahdavi. Rapid treatment planning for low-dose-rate prostate brachytherapy with tp-gan. In *International Conference on Medical Image Computing and Computer-Assisted Intervention*, pages 581–590. Springer.
- [5] Amanda M Aleong, Alejandro Berlin, Jette Borg, Joelle Helou, Akbar Beiki-Ardakani, Alexandra Rink, Srinivas Raman, Peter Chung, and Robert A Weersink. Rapid multi-catheter segmentation for magnetic resonance image-guided catheter-based interventions. *Medical Physics*, 2024. ISSN 0094-2405.
- [6] D. Allman, A. Reiter, and M. A. L. Bell. Photoacoustic source detection and reflection artifact removal enabled by deep learning. *IEEE Trans Med Imaging*, 37(6):1464–1477, 2018. ISSN 1558-254X (Electronic) 0278-0062 (Print) 0278-0062 (Linking). doi: 10.1109/TMI.2018.2829662. URL <https://www.ncbi.nlm.nih.gov/pubmed/29870374>.
- [7] Emran Mohammad Abu Anas, Saman Nouranian, S. Sara Mahdavi, Ingrid Spadinger, William J. Morris, Septimu E. Salcudean, Parvin Mousavi, and Purang Abolmaesumi. Clinical target-volume delineation in prostate brachytherapy using residual neural networks. *Medical Image*

Computing and Computer Assisted Intervention-MICCAI 2017, pages 365–373. Springer International Publishing. ISBN 978-3-319-66179-7.

- [8] C. Andersen, T. Ryden, P. Thunberg, and J. H. Lagerlof. Deep learning-based digitization of prostate brachytherapy needles in ultrasound images. *Med Phys*, 47(12):6414–6420, 2020. ISSN 2473-4209 (Electronic) 0094-2405 (Print) 0094-2405 (Linking). doi: 10.1002/mp.14508. URL <https://www.ncbi.nlm.nih.gov/pubmed/33012023>.
- [9] F. Berumen, S. A. Enger, and L. Beaulieu. Fastd(m,m)calculation in ldr brachytherapy using deep learning methods. *Phys Med Biol*, 68(11), 2023. ISSN 1361-6560 (Electronic) 0031-9155 (Linking). doi: 10.1088/1361-6560/accd42. URL <https://www.ncbi.nlm.nih.gov/pubmed/37059110>.
- [10] N. Bousson, U. Schick, G. Dissaux, L. Ollivier, G. Goasduff, O. Pradier, A. Valeri, and D. Visvikis. A machine-learning approach based on 409 treatments to predict optimal number of iodine-125 seeds in low-dose-rate prostate brachytherapy. *J Contemp Brachytherapy*, 13(5):541–548, 2021. ISSN 1689-832X (Print) 2081-2841 (Electronic) 2081-2841 (Linking). doi: 10.5114/jcb.2021.109789. URL <https://www.ncbi.nlm.nih.gov/pubmed/34759979>.
- [11] Yufeng Cao, April Vasantachart, Omar Ragab, Shelly Bian, Priya Mitra, Zhengzheng Xu, Audrey Zhuang Gallogly, Jing Cui, Zhilei Liu Shen, and Salim Balik. Automatic segmentation of high-risk clinical target volume for tandem-and-ovoids brachytherapy patients using an asymmetric dual-path convolutional neural network. *Medical physics*, 49(3):1712–1722, 2022. ISSN 0094-2405.
- [12] Jui-Hung Chang, Kai-Hsiang Lin, Ti-Hao Wang, Yu-Kai Zhou, and Pau-Choo Chung. Image segmentation in 3d brachytherapy using convolutional lstm. *Journal of Medical and Biological Engineering*, 41:636–651, 2021. ISSN 1609-0985.
- [13] Cyrus Chargari, Eric Deutsch, Pierre Blanchard, Sebastien Gouy, Hélène Martelli, Florent Guérin, Isabelle Dumas, Alberto Bossi, Philippe Morice, and Akila N Viswanathan. Brachytherapy: An overview for clinicians. *CA: a cancer journal for clinicians*, 69(5):386–401, 2019. ISSN 0007-9235.
- [14] J. Chen, H. Chen, Z. Zhong, Z. Wang, B. Hrycushko, L. Zhou, S. Jiang, K. Albuquerque, X. Gu, and X. Zhen. Investigating rectal toxicity associated dosimetric features with deformable accumulated rectal surface dose maps for cervical cancer radiotherapy. *Radiat Oncol*, 13(1):125, 2018. ISSN 1748-717X (Electronic) 1748-717X (Linking). doi: 10.1186/s13014-018-1068-0. URL <https://www.ncbi.nlm.nih.gov/pubmed/29980214>.
- [15] Jieneng Chen, Yongyi Lu, Qihang Yu, Xiangde Luo, Ehsan Adeli, Yan Wang, Le Lu, Alan L Yuille, and Yuyin Zhou. Transunet: Transformers make strong encoders for medical image segmentation. *arXiv preprint arXiv:2102.04306*, 2021.
- [16] S Chen, S Shen, EA Simiele, Z Iqbal, DN Stanley, X Wu, J Peacock, MB Yusuf, S Marcrom, and C Cardenas. Artificial intelligence-assisted automated applicator digitization for fully-automated gynecological high-dose rate brachytherapy treatment planning. *International Journal of Radiation Oncology, Biology, Physics*, 117(2):e651–e652, 2023. ISSN 0360-3016.
- [17] Y. Chen, L. Xing, L. Yu, W. Liu, B. Pooya Fahimian, T. Niedermayr, H. P. Bagshaw, M. Buyyounouski, and B. Han. Mr to ultrasound image registration with segmentation-based learning for hdr prostate brachytherapy. *Med Phys*, 48(6):3074–3083, 2021. ISSN 2473-4209 (Electronic) 0094-2405 (Linking). doi: 10.1002/mp.14901. URL <https://www.ncbi.nlm.nih.gov/pubmed/33905566>.
- [18] K. G. Cortes, K. Kallis, A. Simon, J. Mayadev, S. M. Meyers, and K. L. Moore. Knowledge-based three-dimensional dose prediction for tandem-and-ovoid brachytherapy. *Brachytherapy*, 21(4): 532–542, 2022. ISSN 1873-1449 (Electronic) 1538-4721 (Linking). doi: 10.1016/j.brachy.2022.03.002. URL <https://www.ncbi.nlm.nih.gov/pubmed/35562285>.
- [19] X. Dai, Y. Lei, Y. Zhang, R. L. J. Qiu, T. Wang, S. A. Dresser, W. J. Curran, P. Patel, T. Liu, and X. Yang. Automatic multi-catheter detection using deeply supervised convolutional neural network in mri-guided hdr prostate brachytherapy. *Med Phys*, 47(9):4115–4124, 2020. ISSN 2473-4209 (Electronic) 0094-2405 (Print) 0094-2405 (Linking). doi: 10.1002/mp.14307. URL <https://www.ncbi.nlm.nih.gov/pubmed/32484573>.

- [20] D Jeffrey Demanes, Sheila Rege, Rodney R Rodriguez, Kathleen L Schutz, Gillian A Altieri, and Thomas Wong. The use and advantages of a multichannel vaginal cylinder in high-dose-rate brachytherapy. *International Journal of Radiation Oncology* Biology* Physics*, 44(1):211–219, 1999. ISSN 0360-3016.
- [21] Christopher L Deufel, Shulan Tian, Benjamin B Yan, Birjoo D Vaishnav, Michael G Haddock, and Ivy A Petersen. Automated applicator digitization for high-dose-rate cervix brachytherapy using image thresholding and density-based clustering. *Brachytherapy*, 19(1):111–118, 2020. ISSN 1538-4721.
- [22] Xue Dong, Yang Lei, Sibao Tian, Tonghe Wang, Pretesh Patel, Walter J Curran, Ashesh B Jani, Tian Liu, and Xiaofeng Yang. Synthetic mri-aided multi-organ segmentation on male pelvic ct using cycle consistent deep attention network. *Radiotherapy and Oncology*, 141:192–199, 2019. ISSN 0167-8140.
- [23] J. Duan, C. E. Vargas, N. Y. Yu, B. S. Laughlin, D. S. Toesca, S. Keole, J. C. M. Rwigema, W. W. Wong, S. E. Schild, X. Feng, Q. Chen, and Y. Rong. Incremental retraining, clinical implementation, and acceptance rate of deep learning auto-segmentation for male pelvis in a multiuser environment. *Med Phys*, 50(7):4079–4091, 2023. ISSN 2473-4209 (Electronic) 0094-2405 (Linking). doi: 10.1002/mp.16537. URL <https://www.ncbi.nlm.nih.gov/pubmed/37287322>.
- [24] Richard O Duda and Peter E Hart. Use of the hough transformation to detect lines and curves in pictures. *Communications of the ACM*, 15(1):11–15, 1972. ISSN 0001-0782.
- [25] D. Duprez, C. Trauernicht, H. Simonds, and O. Williams. Self-configuring nnu-net for automatic delineation of the organs at risk and target in high-dose rate cervical brachytherapy, a low/middle-income country’s experience. *J Appl Clin Med Phys*, 24(8):e13988, 2023. ISSN 1526-9914 (Electronic) 1526-9914 (Linking). doi: 10.1002/acm2.13988. URL <https://www.ncbi.nlm.nih.gov/pubmed/37042449>.
- [26] S. Ecker, L. Zimmermann, G. Heilemann, Y. Niatsetski, M. Schmid, A. E. Sturdza, J. Knoth, C. Kirisits, and N. Nesvacil. Neural network-assisted automated image registration for mri-guided adaptive brachytherapy in cervical cancer. *Z Med Phys*, 32(4):488–499, 2022. ISSN 1876-4436 (Electronic) 0939-3889 (Print) 0939-3889 (Linking). doi: 10.1016/j.zemedi.2022.04.002. URL <https://www.ncbi.nlm.nih.gov/pubmed/35570099>.
- [27] Issam El Naqa and Martin J Murphy. *What is machine learning?* Springer, 2015. ISBN 3319183044.
- [28] Jiawei Fan, Lei Xing, and Yong Yang. Independent verification of brachytherapy treatment plan by using deep learning inference modeling. *Physics in Medicine & Biology*, 66(12):125014, 2021. ISSN 0031-9155.
- [29] Yabo Fu, Hao Zhang, Eric D Morris, Carri K Glide-Hurst, Suraj Pai, Alberto Traverso, Leonard Wee, Ibrahim Hadzic, Per-Ivar Lønne, and Chenyang Shen. Artificial intelligence in radiation therapy. *IEEE transactions on radiation and plasma medical sciences*, 6(2):158–181, 2021. ISSN 2469-7311.
- [30] Yin Gao, Yesenia Gonzalez, Chika Nwachukwu, Kevin Albuquerque, and Xun Jia. Predicting treatment plan approval probability for high-dose-rate brachytherapy of cervical cancer using adversarial deep learning. *Physics in Medicine & Biology*, 69(9):095010, 2024. ISSN 0031-9155.
- [31] S. Ghosh, K. Punithakumar, F. Huang, G. Menon, and P. Boulanger. Deep learning using pre-brachytherapy mri to automatically predict applicator induced complex uterine deformation. *Annu Int Conf IEEE Eng Med Biol Soc*, 2022:3826–3829, 2022. ISSN 2694-0604 (Electronic) 2375-7477 (Linking). doi: 10.1109/EMBC48229.2022.9871157. URL <https://www.ncbi.nlm.nih.gov/pubmed/36086328>.
- [32] Derek J Gillies, Jessica R Rodgers, Igor Gyacskov, Priyanka Roy, Nirmal Kakani, Derek W Cool, and Aaron Fenster. Deep learning segmentation of general interventional tools in two-dimensional ultrasound images. *Medical Physics*, 47(10):4956–4970, 2020. ISSN 0094-2405.

- [33] K. B. Girum, A. Lalande, R. Hussain, and G. Crehange. A deep learning method for real-time intraoperative us image segmentation in prostate brachytherapy. *Int J Comput Assist Radiol Surg*, 15(9):1467–1476, 2020. ISSN 1861-6429 (Electronic) 1861-6410 (Linking). doi: 10.1007/s11548-020-02231-x. URL <https://www.ncbi.nlm.nih.gov/pubmed/32691302>.
- [34] Kibrom Berihu Girum, Gilles Créhange, Raabid Hussain, and Alain Lalande. Fast interactive medical image segmentation with weakly supervised deep learning method. *International Journal of Computer Assisted Radiology and Surgery*, 15:1437–1444, 2020. ISSN 1861-6410.
- [35] M. Golshan, D. Karimi, S. Mahdavi, J. Lobo, M. Peacock, S. E. Salcudean, and I. Spadinger. Automatic detection of brachytherapy seeds in 3d ultrasound images using a convolutional neural network. *Phys Med Biol*, 65(3):035016, 2020. ISSN 1361-6560 (Electronic) 0031-9155 (Linking). doi: 10.1088/1361-6560/ab64b5. URL <https://www.ncbi.nlm.nih.gov/pubmed/31860899>.
- [36] Ian Goodfellow, Jean Pouget-Abadie, Mehdi Mirza, Bing Xu, David Warde-Farley, Sherjil Ozair, Aaron Courville, and Yoshua Bengio. Generative adversarial networks. *Communications of the ACM*, 63(11):139–144, 2020. ISSN 0001-0782.
- [37] Christopher D Goodman, Hatim Fakir, Stephen Pautler, Joseph Chin, and Glenn S Bauman. Dosimetric evaluation of psm a pet-delineated dominant intraprostatic lesion simultaneous infield boosts. *Advances in radiation oncology*, 5(2):212–220, 2020. ISSN 2452-1094.
- [38] Peter Grimm, Ignace Billiet, David Bostwick, Adam P Dicker, Steven Frank, Jos Immerzeel, Mira Keyes, Patrick Kupelian, W Robert Lee, and Stefan Machtens. Comparative analysis of prostate-specific antigen free survival outcomes for patients with low, intermediate and high risk prostate cancer treatment by radical therapy. results from the prostate cancer results study group. *BJU international*, 109:22–29, 2012. ISSN 1464-4096.
- [39] Hanxue Gu, Haoyu Dong, Jichen Yang, and Maciej A Mazurowski. How to build the best medical image segmentation algorithm using foundation models: a comprehensive empirical study with segment anything model. *arXiv preprint arXiv:2404.09957*, 2024.
- [40] P. Hampole, T. Harding, D. Gillies, N. Orlando, C. Edirisinghe, L. C. Mendez, D. D’Souza, V. Velker, R. Correa, J. Helou, S. Xing, A. Fenster, and D. A. Hoover. Deep learning-based ultrasound auto-segmentation of the prostate with brachytherapy implanted needles. *Med Phys*, 51(4):2665–2677, 2024. ISSN 2473-4209 (Electronic) 0094-2405 (Linking). doi: 10.1002/mp.16811. URL <https://www.ncbi.nlm.nih.gov/pubmed/37888789>.
- [41] Ali Hatamizadeh, Yucheng Tang, Vishwesh Nath, Dong Yang, Andriy Myronenko, Bennett Landman, Holger R Roth, and Daguang Xu. Unetr: Transformers for 3d medical image segmentation. In *Proceedings of the IEEE/CVF winter conference on applications of computer vision*, pages 574–584.
- [42] Sheng He, Rina Bao, P Ellen Grant, and Yangming Ou. U-netmer: U-net meets transformer for medical image segmentation. *arXiv preprint arXiv:2304.01401*, 2023.
- [43] Xiuxiu He, Yang Lei, Yingzi Liu, Zhen Tian, Tonghe Wang, Walter J Curran, Tian Liu, and Xiaofeng Yang. Deep attentional gan-based high-resolution ultrasound imaging. In *Medical Imaging 2020: Ultrasonic Imaging and Tomography*, volume 11319, pages 61–66. SPIE.
- [44] TP Hellebust. Place of modern imaging in brachytherapy planning. *Cancer/Radiothérapie*, 22(4): 326–333, 2018. ISSN 1278-3218.
- [45] O. Hoffer, T. Rabin, R. R. Nir, R. Y. Brzezinski, Y. Zimmer, and I. Gannot. Automated thermal imaging monitors the local response to cervical cancer brachytherapy. *J Biophotonics*, 16(1):e202200214, 2023. ISSN 1864-0648 (Electronic) 1864-063X (Linking). doi: 10.1002/jbio.202200214. URL <https://www.ncbi.nlm.nih.gov/pubmed/36063415>.
- [46] Edward J Holupka, John Rossman, Tye Morancy, Joseph Aronovitz, and Irving D Kaplan. The detection of implanted radioactive seeds on ultrasound images using convolution neural networks. 2022.

- [47] W. T. Hrinivich, M. Morcos, A. Viswanathan, and J. Lee. Automatic tandem and ring reconstruction using mri for cervical cancer brachytherapy. *Med Phys*, 46(10):4324–4332, 2019. ISSN 2473-4209 (Electronic) 0094-2405 (Linking). doi: 10.1002/mp.13730. URL <https://www.ncbi.nlm.nih.gov/pubmed/31329302>.
- [48] H. Hu, Q. Yang, J. Li, P. Wang, B. Tang, X. Wang, and J. Lang. Deep learning applications in automatic segmentation and reconstruction in ct-based cervix brachytherapy. *J Contemp Brachytherapy*, 13(3):325–330, 2021. ISSN 1689-832X (Print) 2081-2841 (Electronic) 2081-2841 (Linking). doi: 10.5114/jcb.2021.106118. URL <https://www.ncbi.nlm.nih.gov/pubmed/34122573>.
- [49] Zoe Hu, Harry Brastianos, Tamas Ungi, Csaba Pinter, Tim Olding, Martin Korzeniowski, and Gabor Fichtinger. Automated catheter segmentation using 3d ultrasound images in high-dose-rate prostate brachytherapy. In *Medical Imaging 2021: Image-Guided Procedures, Robotic Interventions, and Modeling*, volume 11598, pages 252–259. SPIE.
- [50] Mingxu Huang, Chaolu Feng, Deyu Sun, Ming Cui, and Dazhe Zhao. Segmentation of clinical target volume from ct images for cervical cancer using deep learning. *Technology in Cancer Research & Treatment*, 22:15330338221139164, 2023. ISSN 1533-0346.
- [51] X. Huang, J. Wang, F. Tang, T. Zhong, and Y. Zhang. Metal artifact reduction on cervical ct images by deep residual learning. *Biomed Eng Online*, 17(1):175, 2018. ISSN 1475-925X (Electronic) 1475-925X (Linking). doi: 10.1186/s12938-018-0609-y. URL <https://www.ncbi.nlm.nih.gov/pubmed/30482231>.
- [52] Elizabeth Huynh, Ahmed Hosny, Christian Guthier, Danielle S Bitterman, Steven F Petit, Daphne A Haas-Kogan, Benjamin Kann, Hugo JWL Aerts, and Raymond H Mak. Artificial intelligence in radiation oncology. *Nature Reviews Clinical Oncology*, 17(12):771–781, 2020. ISSN 1759-4774.
- [53] Fabian Isensee, Jens Petersen, Andre Klein, David Zimmerer, Paul F Jaeger, Simon Kohl, Jakob Wasserthal, Gregor Koehler, Tobias Norajitra, and Sebastian Wirkert. nnu-net: Self-adapting framework for u-net-based medical image segmentation. *arXiv preprint arXiv:1809.10486*, 2018.
- [54] Phillip Isola, Jun-Yan Zhu, Tinghui Zhou, and Alexei A Efros. Image-to-image translation with conditional adversarial networks. In *Proceedings of the IEEE conference on computer vision and pattern recognition*, pages 1125–1134.
- [55] R. Jaber, Z. Siavashpour, M. R. Aghamiri, C. Kirisits, and R. Ghaderi. Artificial neural network based gynaecological image-guided adaptive brachytherapy treatment planning correction of intra-fractional organs at risk dose variation. *J Contemp Brachytherapy*, 9(6):508–518, 2017. ISSN 1689-832X (Print) 2081-2841 (Electronic) 2081-2841 (Linking). doi: 10.5114/jcb.2017.72567. URL <https://www.ncbi.nlm.nih.gov/pubmed/29441094>.
- [56] X. Jiang, F. Wang, Y. Chen, and S. Yan. Refinenet-based automatic delineation of the clinical target volume and organs at risk for three-dimensional brachytherapy for cervical cancer. *Ann Transl Med*, 9(23):1721, 2021. ISSN 2305-5839 (Print) 2305-5847 (Electronic) 2305-5839 (Linking). doi: 10.21037/atm-21-4074. URL <https://www.ncbi.nlm.nih.gov/pubmed/35071415>.
- [57] H. Jung, Y. Gonzalez, C. Shen, P. Klages, K. Albuquerque, and X. Jia. Deep-learning-assisted automatic digitization of applicators in 3d ct image-based high-dose-rate brachytherapy of gynecological cancer. *Brachytherapy*, 18(6):841–851, 2019. ISSN 1873-1449 (Electronic) 1538-4721 (Linking). doi: 10.1016/j.brachy.2019.06.003. URL <https://www.ncbi.nlm.nih.gov/pubmed/31345749>.
- [58] Hyunuk Jung, Chenyang Shen, Yesenia Gonzalez, Kevin Albuquerque, and Xun Jia. Deep-learning assisted automatic digitization of interstitial needles in 3d ct image based high dose-rate brachytherapy of gynecological cancer. *Physics in Medicine & Biology*, 64(21):215003, 2019. ISSN 0031-9155.
- [59] Hyejoo Kang, Alexander R Podgorsak, Bhanu Prasad Venkatesulu, Anjali L Saripalli, Brian Chou, Abhishek A Solanki, Matthew Harkenrider, Steven Shea, John C Roeske, and Mohammed Abuhamad. Prostate segmentation accuracy using synthetic mri for high-dose-rate prostate brachytherapy treatment planning. *Physics in Medicine & Biology*, 68(15):155017, 2023. ISSN 0031-9155.

- [60] D. Karimi, Q. Zeng, P. Mathur, A. Avinash, S. Mahdavi, I. Spadinger, P. Abolmaesumi, and S. E. Salcudean. Accurate and robust deep learning-based segmentation of the prostate clinical target volume in ultrasound images. *Med Image Anal*, 57:186–196, 2019. ISSN 1361-8423 (Electronic) 1361-8415 (Linking). doi: 10.1016/j.media.2019.07.005. URL <https://www.ncbi.nlm.nih.gov/pubmed/31325722>.
- [61] Gayoung Kim, Majd Antaki, Ehud J Schmidt, Michael Roumeliotis, Akila N Viswanathan, and Junghoon Lee. Intraoperative mri-guided cervical cancer brachytherapy with automatic tissue segmentation using dual convolution-transformer network and real-time needle tracking. In *Medical Imaging 2024: Image-Guided Procedures, Robotic Interventions, and Modeling*, volume 12928, pages 263–270. SPIE.
- [62] M. T. King, C. E. Kehayias, T. Chaunzwa, D. B. Rosen, A. R. Mahal, T. D. Wallburn, M. G. Milligan, M. A. Dyer, P. L. Nguyen, P. F. Orio, T. C. Harris, I. Buzurovic, and C. V. Guthier. Observer preference of artificial intelligence-generated versus clinical prostate contours for ultrasound-based high dose rate brachytherapy. *Med Phys*, 50(10):5935–5943, 2023. ISSN 2473-4209 (Electronic) 0094-2405 (Linking). doi: 10.1002/mp.16716. URL <https://www.ncbi.nlm.nih.gov/pubmed/37665729>.
- [63] Alexander Kirillov, Eric Mintun, Nikhila Ravi, Hanzi Mao, Chloe Rolland, Laura Gustafson, Tete Xiao, Spencer Whitehead, Alexander C Berg, and Wan-Yen Lo. Segment anything. In *Proceedings of the IEEE/CVF International Conference on Computer Vision*, pages 4015–4026.
- [64] Abigayle C Kraus, Zohaib Iqbal, Rex A Cardan, Richard A Popple, Dennis N Stanley, Sui Shen, Joel A Pogue, Xingen Wu, Kevin Lee, and Samuel Marcrom. Prospective evaluation of automated contouring for ct-based brachytherapy for gynecologic malignancies. *Advances in Radiation Oncology*, 9(4):101417, 2024. ISSN 2452-1094.
- [65] Y. Lei, S. Tian, X. He, T. Wang, B. Wang, P. Patel, A. B. Jani, H. Mao, W. J. Curran, T. Liu, and X. Yang. Ultrasound prostate segmentation based on multidirectional deeply supervised v-net. *Med Phys*, 46(7):3194–3206, 2019. ISSN 2473-4209 (Electronic) 0094-2405 (Print) 0094-2405 (Linking). doi: 10.1002/mp.13577. URL <https://www.ncbi.nlm.nih.gov/pubmed/31074513>.
- [66] Y. Lei, T. Wang, Y. Fu, J. Roper, A. B. Jani, T. Liu, P. Patel, and X. Yang. Catheter position prediction using deep-learning-based multi-atlas registration for high-dose rate prostate brachytherapy. *Med Phys*, 48(11):7261–7270, 2021. ISSN 2473-4209 (Electronic) 0094-2405 (Print) 0094-2405 (Linking). doi: 10.1002/mp.15206. URL <https://www.ncbi.nlm.nih.gov/pubmed/34480801>.
- [67] Yang Lei, Xue Dong, Zhen Tian, Yingzi Liu, Sibao Tian, Tonghe Wang, Xiaojun Jiang, Pretesh Patel, Ashesh B Jani, and Hui Mao. Ct prostate segmentation based on synthetic mri-aided deep attention fully convolution network. *Medical physics*, 47(2):530–540, 2020. ISSN 0094-2405.
- [68] Yang Lei, Tonghe Wang, Justin Roper, Ashesh B Jani, Sagar A Patel, Walter J Curran, Pretesh Patel, Tian Liu, and Xiaofeng Yang. Male pelvic multi-organ segmentation on transrectal ultrasound using anchor-free mask cnn. *Medical Physics*, 48(6):3055–3064, 2021. ISSN 0094-2405.
- [69] Y. Li, M. R. Imami, L. Zhao, A. Amindarolzari, E. Mena, J. Leal, J. Chen, A. Gafita, A. F. Voter, X. Li, Y. Du, C. Zhu, P. L. Choyke, B. Zou, Z. Jiao, S. P. Rowe, M. G. Pomper, and H. X. Bai. An automated deep learning-based framework for uptake segmentation and classification on psma pet/ct imaging of patients with prostate cancer. *J Imaging Inform Med*, 2024. ISSN 2948-2933 (Electronic) 2948-2925 (Linking). doi: 10.1007/s10278-024-01104-y. URL <https://www.ncbi.nlm.nih.gov/pubmed/38587770>.
- [70] Z. Li, Q. Zhu, L. Zhang, X. Yang, Z. Li, and J. Fu. A deep learning-based self-adapting ensemble method for segmentation in gynecological brachytherapy. *Radiat Oncol*, 17(1):152, 2022. ISSN 1748-717X (Electronic) 1748-717X (Linking). doi: 10.1186/s13014-022-02121-3. URL <https://www.ncbi.nlm.nih.gov/pubmed/36064571>.
- [71] Z. Li, Z. Yang, J. Lu, Q. Zhu, Y. Wang, M. Zhao, Z. Li, and J. Fu. Deep learning-based dose map prediction for high-dose-rate brachytherapy. *Phys Med Biol*, 68(17), 2023. ISSN 1361-6560 (Electronic) 0031-9155 (Linking). doi: 10.1088/1361-6560/acecd2. URL <https://www.ncbi.nlm.nih.gov/pubmed/37589292>.

- [72] H. M. Linares Rosales, G. Couture, L. Archambault, S. Beddar, P. Despres, and L. Beaulieu. On the use of machine learning methods for mpsd calibration in hdr brachytherapy. *Phys Med*, 91:73–79, 2021. ISSN 1724-191X (Electronic) 1120-1797 (Linking). doi: 10.1016/j.ejmp.2021.10.003. URL <https://www.ncbi.nlm.nih.gov/pubmed/34717139>.
- [73] Derek Liu, Shayantonee Tupor, Jaskaran Singh, Trey Chernoff, Nelson Leong, Evgeny Sadikov, Asim Amjad, and Sandra Zilles. The challenges facing deep learning–based catheter localization for ultrasound guided high-dose-rate prostate brachytherapy. *Medical Physics*, 49(4):2442–2451, 2022. ISSN 0094-2405.
- [74] Jonathan Long, Evan Shelhamer, and Trevor Darrell. Fully convolutional networks for semantic segmentation. In *Proceedings of the IEEE conference on computer vision and pattern recognition*, pages 3431–3440.
- [75] J Nicholas Lukens, Mauricio Gamez, Kenneth Hu, and Louis B Harrison. Modern brachytherapy. In *Seminars in oncology*, volume 41, pages 831–847. Elsevier. ISBN 0093-7754.
- [76] Jun Ma, Yuting He, Feifei Li, Lin Han, Chenyu You, and Bo Wang. Segment anything in medical images. *Nature Communications*, 15(1):654, 2024. ISSN 2041-1723.
- [77] X. Mao, J. Pineau, R. Keyes, and S. A. Enger. Rapidbrachydl: Rapid radiation dose calculations in brachytherapy via deep learning. *Int J Radiat Oncol Biol Phys*, 108(3):802–812, 2020. ISSN 1879-355X (Electronic) 0360-3016 (Linking). doi: 10.1016/j.ijrobp.2020.04.045. URL <https://www.ncbi.nlm.nih.gov/pubmed/32413546>.
- [78] L. A. Matkovic, T. Wang, Y. Lei, O. O. Akin-Akintayo, O. A. Abiodun Ojo, A. A. Akintayo, J. Roper, J. D. Bradley, T. Liu, D. M. Schuster, and X. Yang. Prostate and dominant intraprostatic lesion segmentation on pet/ct using cascaded regional-net. *Phys Med Biol*, 66(24), 2021. ISSN 1361-6560 (Electronic) 0031-9155 (Print) 0031-9155 (Linking). doi: 10.1088/1361-6560/ac3c13. URL <https://www.ncbi.nlm.nih.gov/pubmed/34808603>.
- [79] R. Mohammadi, I. Shokatian, M. Salehi, H. Arabi, I. Shiri, and H. Zaidi. Deep learning-based auto-segmentation of organs at risk in high-dose rate brachytherapy of cervical cancer. *Radiother Oncol*, 159:231–240, 2021. ISSN 1879-0887 (Electronic) 0167-8140 (Linking). doi: 10.1016/j.radonc.2021.03.030. URL <https://www.ncbi.nlm.nih.gov/pubmed/33831446>.
- [80] K. Nakanishi, S. Yamamoto, T. Yabe, K. Yogo, Y. Noguchi, K. Okudaira, N. Kawachi, and J. Kataoka. Estimating blurless and noise-free ir-192 source images from gamma camera images for high-dose-rate brachytherapy using a deep-learning approach. *Biomed Phys Eng Express*, 10(1), 2023. ISSN 2057-1976 (Electronic) 2057-1976 (Linking). doi: 10.1088/2057-1976/ad0bb2. URL <https://www.ncbi.nlm.nih.gov/pubmed/37948761>.
- [81] H. G. Nguyen, C. Fouard, and J. Troccaz. Segmentation, separation and pose estimation of prostate brachytherapy seeds in ct images. *IEEE Trans Biomed Eng*, 62(8):2012–24, 2015. ISSN 1558-2531 (Electronic) 0018-9294 (Linking). doi: 10.1109/TBME.2015.2409304. URL <https://www.ncbi.nlm.nih.gov/pubmed/25769143>.
- [82] Ruiyan Ni, Kathy Han, Benjamin Haibe-Kains, and Alexandra Rink. Generalizability of deep learning in organ-at-risk segmentation: A transfer learning study in cervical brachytherapy. *Radiotherapy and Oncology*, 197:110332, 2024. ISSN 0167-8140.
- [83] Alexandru Nicolae, Gerard Morton, Hans Chung, Andrew Loblaw, Suneil Jain, Darren Mitchell, Lin Lu, Joelle Helou, Motasem Al-Hanaqta, and Emily Heath. Evaluation of a machine-learning algorithm for treatment planning in prostate low-dose-rate brachytherapy. *International Journal of Radiation Oncology* Biology* Physics*, 97(4):822–829, 2017. ISSN 0360-3016.
- [84] Alexandru Nicolae, Mark Semple, Lin Lu, Mackenzie Smith, Hans Chung, Andrew Loblaw, Gerard Morton, Lucas Castro Mendez, Chia-Lin Tseng, and Melanie Davidson. Conventional vs machine learning–based treatment planning in prostate brachytherapy: results of a phase i randomized controlled trial. *Brachytherapy*, 19(4):470–476, 2020. ISSN 1538-4721.

- [85] Reyhaneh Nosrati, Abraam Soliman, Habib Safigholi, Masoud Hashemi, Matthew Wronski, Gerard Morton, Ana Pejović-Milić, Greg Stanisz, and William Y Song. Mri-based automated detection of implanted low dose rate (ldr) brachytherapy seeds using quantitative susceptibility mapping (qsm) and unsupervised machine learning (ml). *Radiotherapy and Oncology*, 129(3): 540–547, 2018. ISSN 0167-8140.
- [86] S. Nouranian, M. Ramezani, I. Spadinger, W. J. Morris, S. E. Salcudean, and P. Abolmaesumi. Learning-based multi-label segmentation of transrectal ultrasound images for prostate brachytherapy. *IEEE Trans Med Imaging*, 35(3):921–32, 2016. ISSN 1558-254X (Electronic) 0278-0062 (Linking). doi: 10.1109/TMI.2015.2502540. URL <https://www.ncbi.nlm.nih.gov/pubmed/26599701>.
- [87] N. Orlando, D. J. Gillies, I. Gyacskov, C. Romagnoli, D. D’Souza, and A. Fenster. Automatic prostate segmentation using deep learning on clinically diverse 3d transrectal ultrasound images. *Med Phys*, 47(6):2413–2426, 2020. ISSN 2473-4209 (Electronic) 0094-2405 (Linking). doi: 10.1002/mp.14134. URL <https://www.ncbi.nlm.nih.gov/pubmed/32166768>.
- [88] N. Orlando, I. Gyacskov, D. J. Gillies, F. Guo, C. Romagnoli, D. D’Souza, D. W. Cool, D. A. Hoover, and A. Fenster. Effect of dataset size, image quality, and image type on deep learning-based automatic prostate segmentation in 3d ultrasound. *Phys Med Biol*, 67(7), 2022. ISSN 1361-6560 (Electronic) 0031-9155 (Linking). doi: 10.1088/1361-6560/ac5a93. URL <https://www.ncbi.nlm.nih.gov/pubmed/35240585>.
- [89] Keiron O’shea and Ryan Nash. An introduction to convolutional neural networks. *arXiv preprint arXiv:1511.08458*, 2015.
- [90] Michelle Oud, Inger-Karine Kolkman-Deurloo, Jan-Willem Mens, Danny Lathouwers, Zoltán Perkó, Ben Heijmen, and Sebastiaan Breedveld. Fast and fully-automated multi-criterial treatment planning for adaptive hdr brachytherapy for locally advanced cervical cancer. *Radiotherapy and oncology*, 148:143–150, 2020. ISSN 0167-8140.
- [91] T. Peng, Y. Dong, G. Di, J. Zhao, T. Li, G. Ren, L. Zhang, and J. Cai. Boundary delineation in transrectal ultrasound images for region of interest of prostate. *Phys Med Biol*, 68(19), 2023. ISSN 1361-6560 (Electronic) 0031-9155 (Linking). doi: 10.1088/1361-6560/acf5c5. URL <https://www.ncbi.nlm.nih.gov/pubmed/37652058>.
- [92] Daniel G Petereit, Steven J Frank, Akila N Viswanathan, Beth Erickson, Patricia Eifel, Paul L Nguyen, and David E Wazer. Brachytherapy: where has it gone? *Journal of Clinical Oncology*, 33(9):980, 2015.
- [93] Max Peters, Marieke J van Son, Marinus A Moerland, Linda GW Kerkmeijer, Wietse SC Eppinga, Richard P Meijer, Jan JW Lagendijk, Taimur T Shah, and Hashim U Ahmed. Mri-guided ultrafocal hdr brachytherapy for localized prostate cancer: median 4-year results of a feasibility study. *International Journal of Radiation Oncology* Biology* Physics*, 104(5):1045–1053, 2019. ISSN 0360-3016.
- [94] Malvika Pillai, Karthik Adapa, Shiva K Das, Lukasz Mazur, John Dooley, Lawrence B Marks, Reid F Thompson, and Bhisamjit S Chera. Using artificial intelligence to improve the quality and safety of radiation therapy. *Journal of the American College of Radiology*, 16(9):1267–1272, 2019. ISSN 1546-1440.
- [95] Alexander R Podgorsak, Bhanu P Venkatesulu, Mohammad Abuhamad, Matthew M Harkenrider, Abhishek A Solanki, John C Roeske, and Hyejoo Kang. Dosimetric and workflow impact of synthetic-mri use in prostate high-dose-rate brachytherapy. *Brachytherapy*, 22(5):686–696, 2023. ISSN 1538-4721.
- [96] Gang Pu, Shan Jiang, Zhiyong Yang, Yuanjing Hu, and Ziqi Liu. Deep reinforcement learning for treatment planning in high-dose-rate cervical brachytherapy. *Physica Medica*, 94:1–7, 2022. ISSN 1120-1797.
- [97] Katarina M Rajković, Jovan Stanković, Miodrag Aćimović, Nina Đukanović, and Borislava Nikolin. Modelling and optimisation of treatment parameters in high-dose-rate mono

- brachytherapy for localised prostate carcinoma using a multilayer artificial neural network and a genetic algorithm: Pilot study. *Computers in Biology and Medicine*, 126:104045, 2020. ISSN 0010-4825.
- [98] Pranav Rajpurkar, Emma Chen, Oishi Banerjee, and Eric J Topol. Ai in health and medicine. *Nature medicine*, 28(1):31–38, 2022. ISSN 1078-8956.
- [99] Dominique Reijtenbagh, Jérémy Godart, Astrid de Leeuw, Yvette Seppenwoolde, Ina Jürgenliemk-Schulz, Jan-Willem Mens, Remi Nout, and Mischa Hoogeman. Multi-center analysis of machine-learning predicted dose parameters in brachytherapy for cervical cancer. *Radiotherapy and Oncology*, 170:169–175, 2022. ISSN 0167-8140.
- [100] Dominique MW Reijtenbagh, Jérémy Godart, Astrid AC de Leeuw, Ina M Jürgenliemk-Schulz, Jan-Willem M Mens, Michèle Hüge, and Mischa S Hoogeman. Multi-center dosimetric predictions to improve plan quality for brachytherapy for cervical cancer treatment. *Radiotherapy and Oncology*, 182:109518, 2023. ISSN 0167-8140.
- [101] Roque Rodríguez Outeiral, Patrick J González, Eva E Schaake, Uulke A van der Heide, and Rita Simões. Deep learning for segmentation of the cervical cancer gross tumor volume on magnetic resonance imaging for brachytherapy. *Radiation Oncology*, 18(1):91, 2023. ISSN 1748-717X.
- [102] Olaf Ronneberger, Philipp Fischer, and Thomas Brox. U-net: Convolutional networks for biomedical image segmentation. In *Medical image computing and computer-assisted intervention—MICCAI 2015: 18th international conference, Munich, Germany, October 5-9, 2015, proceedings, part III 18*, pages 234–241. Springer. ISBN 3319245732.
- [103] M. Salehi, A. Vafaei Sadr, S. R. Mahdavi, H. Arabi, I. Shiri, and R. Reiazi. Deep learning-based non-rigid image registration for high-dose rate brachytherapy in inter-fraction cervical cancer. *J Digit Imaging*, 36(2):574–587, 2023. ISSN 1618-727X (Electronic) 0897-1889 (Print) 0897-1889 (Linking). doi: 10.1007/s10278-022-00732-6. URL <https://www.ncbi.nlm.nih.gov/pubmed/36417026>.
- [104] J. W. Sanders, S. J. Frank, R. J. Kudchadker, T. L. Bruno, and J. Ma. Development and clinical implementation of seednet: A sliding-window convolutional neural network for radioactive seed identification in mri-assisted radiosurgery (mars). *Magn Reson Med*, 81(6):3888–3900, 2019. ISSN 1522-2594 (Electronic) 0740-3194 (Linking). doi: 10.1002/mrm.27677. URL <https://www.ncbi.nlm.nih.gov/pubmed/30737827>.
- [105] J. W. Sanders, G. D. Lewis, H. D. Thames, R. J. Kudchadker, A. M. Venkatesan, T. L. Bruno, J. Ma, M. D. Pagel, and S. J. Frank. Machine segmentation of pelvic anatomy in mri-assisted radiosurgery (mars) for prostate cancer brachytherapy. *Int J Radiat Oncol Biol Phys*, 108(5):1292–1303, 2020. ISSN 1879-355X (Electronic) 0360-3016 (Linking). doi: 10.1016/j.ijrobp.2020.06.076. URL <https://www.ncbi.nlm.nih.gov/pubmed/32634543>.
- [106] J. W. Sanders, R. J. Kudchadker, C. Tang, H. Mok, A. M. Venkatesan, H. D. Thames, and S. J. Frank. Prospective evaluation of prostate and organs at risk segmentation software for mri-based prostate radiation therapy. *Radiol Artif Intell*, 4(2):e210151, 2022. ISSN 2638-6100 (Electronic) 2638-6100 (Linking). doi: 10.1148/ryai.210151. URL <https://www.ncbi.nlm.nih.gov/pubmed/35391775>.
- [107] Amani Shaaer, Moti Paudel, Melanie Davidson, Mark Semple, Alexandru Nicolae, Lucas Castro Mendez, Hans Chung, Andrew Loblaw, Chia-Lin Tseng, and Gerard Morton. Dosimetric evaluation of mri-to-ultrasound automated image registration algorithms for prostate brachytherapy. *Brachytherapy*, 19(5):599–606, 2020. ISSN 1538-4721.
- [108] Amani Shaaer, Moti Paudel, Mackenzie Smith, Frances Tonolet, and Ananth Ravi. Deep-learning-assisted algorithm for catheter reconstruction during mr-only gynecological interstitial brachytherapy. *Journal of Applied Clinical Medical Physics*, 23(2):e13494, 2022. ISSN 1526-9914.
- [109] Mohammed Yousef Shaheen. Applications of artificial intelligence (ai) in healthcare: A review. *ScienceOpen Preprints*, 2021.

- [110] Chenyang Shen, Yesenia Gonzalez, Peter Klages, Nan Qin, Hyunuk Jung, Liyuan Chen, Dan Nguyen, Steve B Jiang, and Xun Jia. Intelligent inverse treatment planning via deep reinforcement learning, a proof-of-principle study in high dose-rate brachytherapy for cervical cancer. *Physics in Medicine & Biology*, 64(11):115013, 2019. ISSN 0031-9155.
- [111] Janusz Skowronek. Current status of brachytherapy in cancer treatment—short overview. *Journal of contemporary brachytherapy*, 9(6):581–589, 2017. ISSN 1689-832X.
- [112] Xinrui Song, Hengtao Guo, Xuanang Xu, Hanqing Chao, Sheng Xu, Baris Turkbey, Bradford J Wood, Ge Wang, and Pingkun Yan. Cross-modal attention for mri and ultrasound volume registration. In *Medical Image Computing and Computer Assisted Intervention—MICCAI 2021: 24th International Conference, Strasbourg, France, September 27–October 1, 2021, Proceedings, Part IV 24*, pages 66–75. Springer. ISBN 3030872017.
- [113] Kailyn Stenhouse, Michael Roumeliotis, Philip Ciunkiewicz, Robyn Banerjee, Svetlana Yanushkevich, and Philip McGeachy. Development of a machine learning model for optimal applicator selection in high-dose-rate cervical brachytherapy. *Frontiers in Oncology*, 11:611437, 2021. ISSN 2234-943X.
- [114] M. Styner, C. Brechbuhler, G. Szekely, and G. Gerig. Parametric estimate of intensity inhomogeneities applied to mri. *IEEE Trans Med Imaging*, 19(3):153–65, 2000. ISSN 0278-0062 (Print) 0278-0062 (Linking). doi: 10.1109/42.845174. URL <https://www.ncbi.nlm.nih.gov/pubmed/10875700>.
- [115] Jamema Swamidas, Christian Kirisits, Marisol De Brabandere, Taran Paulsen Hellebust, Frank-André Siebert, and Kari Tanderup. Image registration, contour propagation and dose accumulation of external beam and brachytherapy in gynecological radiotherapy. *Radiotherapy and Oncology*, 143:1–11, 2020. ISSN 0167-8140.
- [116] Christian Szegedy, Wei Liu, Yangqing Jia, Pierre Sermanet, Scott Reed, Dragomir Anguelov, Dumitru Erhan, Vincent Vanhoucke, and Andrew Rabinovich. Going deeper with convolutions. In *Proceedings of the IEEE conference on computer vision and pattern recognition*, pages 1–9.
- [117] Kari Tanderup, Cynthia Ménard, Csaba Polgar, Jacob Christian Lindegaard, Christian Kirisits, and Richard Pötter. Advancements in brachytherapy. *Advanced drug delivery reviews*, 109:15–25, 2017. ISSN 0169-409X.
- [118] Z. Tian, A. Yen, Z. Zhou, C. Shen, K. Albuquerque, and B. Hrycushko. A machine-learning-based prediction model of fistula formation after interstitial brachytherapy for locally advanced gynecological malignancies. *Brachytherapy*, 18(4):530–538, 2019. ISSN 1873-1449 (Electronic) 1538-4721 (Linking). doi: 10.1016/j.brachy.2019.04.004. URL <https://www.ncbi.nlm.nih.gov/pubmed/31103434>.
- [119] G. Valdes, J. M. Luna, E. Eaton, 2nd Simone, C. B., L. H. Ungar, and T. D. Solberg. Mediboost: a patient stratification tool for interpretable decision making in the era of precision medicine. *Sci Rep*, 6:37854, 2016. ISSN 2045-2322 (Electronic) 2045-2322 (Linking). doi: 10.1038/srep37854. URL <https://www.ncbi.nlm.nih.gov/pubmed/27901055>.
- [120] G. Valdes, A. J. Chang, Y. Interian, K. Owen, S. T. Jensen, L. H. Ungar, A. Cunha, T. D. Solberg, and I. C. Hsu. Salvage hdr brachytherapy: Multiple hypothesis testing versus machine learning analysis. *Int J Radiat Oncol Biol Phys*, 101(3):694–703, 2018. ISSN 1879-355X (Electronic) 0360-3016 (Linking). doi: 10.1016/j.ijrobp.2018.03.001. URL <https://www.ncbi.nlm.nih.gov/pubmed/29709315>.
- [121] Eric Vigneault, Khaly Mbodji, Louis-Gabriel Racine, Eric Chevrete, Marie-Claude Lavallée, André-Guy Martin, Philippe Després, and Luc Beaulieu. Image-guided high-dose-rate brachytherapy boost to the dominant intraprostatic lesion using multiparametric magnetic resonance imaging including spectroscopy: results of a prospective study. *Brachytherapy*, 15(6):746–751, 2016. ISSN 1538-4721.
- [122] Mateo Villa, Julien Bert, Antoine Valeri, Ulrike Schick, and Dimitris Visvikis. Fast monte carlo-based inverse planning for prostate brachytherapy by using deep learning. *IEEE Transactions on Radiation and Plasma Medical Sciences*, 6(2):182–188, 2021. ISSN 2469-7311.

- [123] Fuyue Wang, Lei Xing, Hilary Bagshaw, Mark Buyyounouski, and Bin Han. Deep learning applications in automatic needle segmentation in ultrasound-guided prostate brachytherapy. *Medical Physics*, 47(9):3797–3805, 2020. ISSN 0094-2405.
- [124] J. Wang, Y. Chen, Y. Tu, H. Xie, Y. Chen, L. Luo, P. Zhou, and Q. Tang. Evaluation of auto-segmentation for brachytherapy of postoperative cervical cancer using deep learning-based workflow. *Phys Med Biol*, 68(5), 2023. ISSN 1361-6560 (Electronic) 0031-9155 (Linking). doi: 10.1088/1361-6560/acba76. URL <https://www.ncbi.nlm.nih.gov/pubmed/36753762>.
- [125] Shijun Wang and Ronald M Summers. Machine learning and radiology. *Medical image analysis*, 16(5):933–951, 2012. ISSN 1361-8415.
- [126] T. Wang, Y. Lei, E. Schreibmann, J. Roper, T. Liu, D. M. Schuster, A. B. Jani, and X. Yang. Lesion segmentation on (18)f-fluciclovine pet/ct images using deep learning. *Front Oncol*, 13:1274803, 2023. ISSN 2234-943X (Print) 2234-943X (Electronic) 2234-943X (Linking). doi: 10.3389/fonc.2023.1274803. URL <https://www.ncbi.nlm.nih.gov/pubmed/38156106>.
- [127] Tonghe Wang, Robert H Press, Matt Giles, Ashesh B Jani, Peter Rossi, Yang Lei, Walter J Curran, Pretesh Patel, Tian Liu, and Xiaofeng Yang. Multiparametric mri-guided dose boost to dominant intraprostatic lesions in ct-based high-dose-rate prostate brachytherapy. *The British journal of radiology*, 92(1097):20190089, 2019. ISSN 0007-1285.
- [128] Yuenan Wang, Wanwei Jian, Lin Zhu, Chunya Cai, Bailin Zhang, and Xuetao Wang. Attention-gated deep-learning-based automatic digitization of interstitial needles in high-dose-rate brachytherapy for cervical cancer. *Advances in Radiation Oncology*, 9(1):101340, 2024. ISSN 2452-1094.
- [129] L. L. Weishaupt, H. K. Sayed, X. Mao, R. Choo, B. J. Stish, S. A. Enger, and C. Deufel. Approaching automated applicator digitization from a new angle: Using sagittal images to improve deep learning accuracy and robustness in high-dose-rate prostate brachytherapy. *Brachytherapy*, 21(4):520–531, 2022. ISSN 1873-1449 (Electronic) 1538-4721 (Linking). doi: 10.1016/j.brachy.2022.02.005. URL <https://www.ncbi.nlm.nih.gov/pubmed/35422402>.
- [130] Vonetta M Williams, Jenna M Kahn, Nikhil G Thaker, Sushil Beriwal, Paul L Nguyen, Douglas Arthur, Daniel Petereit, and Brandon A Dyer. The case for brachytherapy: why it deserves a renaissance. *Advances in Radiation Oncology*, 6(2):100605, 2021. ISSN 2452-1094.
- [131] Menglin Wu, Xuchen He, Fan Li, Jie Zhu, Shanshan Wang, and Pablo D Burstein. Weakly supervised volumetric prostate registration for mri-trus image driven by signed distance map. *Computers in Biology and Medicine*, 163:107150, 2023. ISSN 0010-4825.
- [132] X. Xu, T. Sanford, B. Turkbey, S. Xu, B. J. Wood, and P. Yan. Polar transform network for prostate ultrasound segmentation with uncertainty estimation. *Med Image Anal*, 78:102418, 2022. ISSN 1361-8423 (Electronic) 1361-8415 (Print) 1361-8415 (Linking). doi: 10.1016/j.media.2022.102418. URL <https://www.ncbi.nlm.nih.gov/pubmed/35349838>.
- [133] Xian Xue, Dazhu Liang, Kaiyue Wang, Jianwei Gao, Jingjing Ding, Fugen Zhou, Juan Xu, Hefeng Liu, Quanfu Sun, and Ping Jiang. A deep learning-based 3d prompt-nnnet model for automatic segmentation in brachytherapy of postoperative endometrial carcinoma. *Journal of Applied Clinical Medical Physics*, page e14371, 2024. ISSN 1526-9914.
- [134] Xin Yi, Ekta Walia, and Paul Babyn. Generative adversarial network in medical imaging: A review. *Medical image analysis*, 58:101552, 2019. ISSN 1361-8415.
- [135] SA Yoganathan, Siji Nojin Paul, Satheesh Paloor, Tarraf Torfeh, Suparna Halsnad Chandramouli, Rabih Hammoud, and Noora Al-Hammadi. Automatic segmentation of magnetic resonance images for high-dose-rate cervical cancer brachytherapy using deep learning. *Medical Physics*, 49(3):1571–1584, 2022. ISSN 0094-2405.
- [136] Hatem Younes, Sandrine Voros, and Jocelyne Troccaz. Automatic needle localization in 3d ultrasound images for brachytherapy. In *2018 IEEE 15th International Symposium on Biomedical Imaging (ISBI 2018)*, pages 1203–1207. IEEE. ISBN 1538636360.

- [137] Hatem Younes, Jocelyne Troccaz, and Sandrine Voros. Machine learning and registration for automatic seed localization in 3d us images for prostate brachytherapy. *Medical Physics*, 48(3): 1144–1156, 2021. ISSN 0094-2405.
- [138] Lang Yu, Wenjun Zhang, Jie Zhang, Qi Chen, Lu Bai, Nan Liu, Tingtian Pang, Bo Yang, and Jie Qiu. A cnn-based dose prediction method for brachytherapy treatment planning of patients with cervical cancer. *Journal of Radiation Research and Applied Sciences*, 17(3):101013, 2024. ISSN 1687-8507.
- [139] T. I. Yusufaly, S. M. Meyers, L. K. Mell, and K. L. Moore. Knowledge-based planning for intact cervical cancer. *Semin Radiat Oncol*, 30(4):328–339, 2020. ISSN 1532-9461 (Electronic) 1053-4296 (Linking). doi: 10.1016/j.semradonc.2020.05.009. URL <https://www.ncbi.nlm.nih.gov/pubmed/32828388>.
- [140] F. Zabihollahy, A. N. Viswanathan, E. J. Schmidt, M. Morcos, and J. Lee. Fully automated multiorgan segmentation of female pelvic magnetic resonance images with coarse-to-fine convolutional neural network. *Med Phys*, 48(11):7028–7042, 2021. ISSN 2473-4209 (Electronic) 0094-2405 (Print) 0094-2405 (Linking). doi: 10.1002/mp.15268. URL <https://www.ncbi.nlm.nih.gov/pubmed/34609756>.
- [141] Fatemeh Zabihollahy, Akila N Viswanathan, Ehud J Schmidt, and Junghoon Lee. Fully automated segmentation of clinical target volume in cervical cancer from magnetic resonance imaging with convolutional neural network. *Journal of applied clinical medical physics*, 23(9):e13725, 2022. ISSN 1526-9914.
- [142] P. Zaffino, G. Pernelle, A. Mastmeyer, A. Mehrtash, H. Zhang, R. Kikinis, T. Kapur, and M. Francesca Spadea. Fully automatic catheter segmentation in mri with 3d convolutional neural networks: application to mri-guided gynecologic brachytherapy. *Phys Med Biol*, 64(16):165008, 2019. ISSN 1361-6560 (Electronic) 0031-9155 (Print) 0031-9155 (Linking). doi: 10.1088/1361-6560/ab2f47. URL <https://www.ncbi.nlm.nih.gov/pubmed/31272095>.
- [143] Nicholas G Zaorsky, Brian J Davis, Paul L Nguyen, Timothy N Showalter, Peter J Hoskin, Yasuo Yoshioka, Gerard C Morton, and Eric M Horwitz. The evolution of brachytherapy for prostate cancer. *Nature Reviews Urology*, 14(7):415–439, 2017. ISSN 1759-4812.
- [144] Q. Zeng, G. Samei, D. Karimi, C. Kesch, S. S. Mahdavi, P. Abolmaesumi, and S. E. Salcudean. Prostate segmentation in transrectal ultrasound using magnetic resonance imaging priors. *Int J Comput Assist Radiol Surg*, 13(6):749–757, 2018. ISSN 1861-6429 (Electronic) 1861-6410 (Linking). doi: 10.1007/s11548-018-1742-6. URL <https://www.ncbi.nlm.nih.gov/pubmed/29589259>.
- [145] Q. Zeng, Y. Fu, Z. Tian, Y. Lei, Y. Zhang, T. Wang, H. Mao, T. Liu, W. J. Curran, A. B. Jani, P. Patel, and X. Yang. Label-driven magnetic resonance imaging (mri)-transrectal ultrasound (trus) registration using weakly supervised learning for mri-guided prostate radiotherapy. *Phys Med Biol*, 65(13):135002, 2020. ISSN 1361-6560 (Electronic) 0031-9155 (Print) 0031-9155 (Linking). doi: 10.1088/1361-6560/ab8cd6. URL <https://www.ncbi.nlm.nih.gov/pubmed/32330922>.
- [146] D. Zhang, Z. Yang, S. Jiang, Z. Zhou, M. Meng, and W. Wang. Automatic segmentation and applicator reconstruction for ct-based brachytherapy of cervical cancer using 3d convolutional neural networks. *J Appl Clin Med Phys*, 21(10):158–169, 2020. ISSN 1526-9914 (Electronic) 1526-9914 (Linking). doi: 10.1002/acm2.13024. URL <https://www.ncbi.nlm.nih.gov/pubmed/32991783>.
- [147] H. W. Zhang, X. M. Zhong, Z. H. Zhang, and H. W. Pang. Dose prediction of organs at risk in patients with cervical cancer receiving brachytherapy using needle insertion based on a neural network method. *BMC Cancer*, 23(1):385, 2023. ISSN 1471-2407 (Electronic) 1471-2407 (Linking). doi: 10.1186/s12885-023-10875-6. URL <https://www.ncbi.nlm.nih.gov/pubmed/37106444>.
- [148] Y. Zhang, X. He, Z. Tian, J. J. Jeong, Y. Lei, T. Wang, Q. Zeng, A. B. Jani, W. J. Curran, P. Patel, T. Liu, and X. Yang. Multi-needle detection in 3d ultrasound images using unsupervised ordergraph regularized sparse dictionary learning. *IEEE Trans Med Imaging*, 39(7):2302–2315, 2020. ISSN 1558-254X (Electronic) 0278-0062 (Print) 0278-0062 (Linking). doi: 10.1109/TMI.2020.2968770. URL <https://www.ncbi.nlm.nih.gov/pubmed/31985414>.

- [149] Y. Zhang, Y. Lei, R. L. J. Qiu, T. Wang, H. Wang, A. B. Jani, W. J. Curran, P. Patel, T. Liu, and X. Yang. Multi-needle localization with attention u-net in us-guided hdr prostate brachytherapy. *Med Phys*, 47(7):2735–2745, 2020. ISSN 2473-4209 (Electronic) 0094-2405 (Print) 0094-2405 (Linking). doi: 10.1002/mp.14128. URL <https://www.ncbi.nlm.nih.gov/pubmed/32155666>.
- [150] Y. Zhang, Z. Tian, Y. Lei, T. Wang, P. Patel, A. B. Jani, W. J. Curran, T. Liu, and X. Yang. Automatic multi-needle localization in ultrasound images using large margin mask rcnn for ultrasound-guided prostate brachytherapy. *Phys Med Biol*, 65(20):205003, 2020. ISSN 1361-6560 (Electronic) 0031-9155 (Linking). doi: 10.1088/1361-6560/aba410. URL <https://www.ncbi.nlm.nih.gov/pubmed/32640435>.
- [151] X. Zhen, J. Chen, Z. Zhong, B. Hrycushko, L. Zhou, S. Jiang, K. Albuquerque, and X. Gu. Deep convolutional neural network with transfer learning for rectum toxicity prediction in cervical cancer radiotherapy: a feasibility study. *Phys Med Biol*, 62(21):8246–8263, 2017. ISSN 1361-6560 (Electronic) 0031-9155 (Linking). doi: 10.1088/1361-6560/aa8d09. URL <https://www.ncbi.nlm.nih.gov/pubmed/28914611>.
- [152] Zongwei Zhou, Md Mahfuzur Rahman Siddiquee, Nima Tajbakhsh, and Jianming Liang. Unet++: A nested u-net architecture for medical image segmentation. In *Deep Learning in Medical Image Analysis and Multimodal Learning for Clinical Decision Support: 4th International Workshop, DLMIA 2018, and 8th International Workshop, ML-CDS 2018, Held in Conjunction with MICCAI 2018, Granada, Spain, September 20, 2018, Proceedings 4*, pages 3–11. Springer. ISBN 3030008886.
- [153] J Zhu, J Yan, J Zhang, L Yu, A Song, Z Zheng, Y Chen, S Wang, Q Chen, and Z Liu. Automatic segmentation of high-risk clinical target volume and organs at risk in brachytherapy of cervical cancer with a convolutional neural network. *Cancer/Radiothérapie*, 2024. ISSN 1278-3218.